

METALLICITY OF THE INTERGALACTIC MEDIUM USING PIXEL STATISTICS: I. METHOD

ANTHONY AGUIRRE AND JOOP SCHAYE
School of Natural Sciences, Institute for Advanced Study, Princeton, NJ 08540
aguirre@ias.edu, schaye@ias.edu

TOM THEUNS
Institute of Astronomy, Madingley Rd., Cambridge CB3 0HA, UK
tt@ast.cam.ac.uk
Draft

ABSTRACT

Studies of absorption spectra of high- z QSOs have revealed that the intergalactic medium at $z \sim 2 - 3$ is enriched to $\sim 10^{-3} - 10^{-2} Z_{\odot}$ for gas densities more than a few times the mean cosmic density, but have not yet produced an accurate metallicity estimate, nor constrained variations in the metallicity with density, redshift, or spatial location. This paper discusses the “pixel optical depth” (POD) method of QSO spectrum analysis, using realistic simulated spectra from cosmological simulations. In this method, absorption in Ly α is compared to corresponding metal absorption on a pixel-by-pixel basis, yielding for each analyzed spectrum a single statistical correlation encoding metal enrichment information. Our simulations allow testing and optimization of each step of the technique’s implementation. Tests show that previous studies have probably been limited by C IV self-contamination and O VI contamination by H I lines; we have developed and tested an effective method of correcting for both contaminants. We summarize these and other findings, and provide a useful recipe for the POD technique’s application to observed spectra. Our tests reveal that the POD technique applied to spectra of presently available quality is effective in recovering useful metallicity information even in underdense gas. We present an extension of the POD technique to directly recover the intergalactic metallicity as a function of gas density. For a given ionizing background, both the oxygen and carbon abundance can be measured with errors of at most a factor of a few over at least an order of magnitude in density, using a single high-quality spectrum.

Subject headings: cosmology: theory — intergalactic medium — quasars: absorption lines

1. INTRODUCTION

Studies of absorption lines in QSO spectra have established that at high redshift ($z \gtrsim 2$) the intergalactic medium (IGM) is enriched by metals to metallicity $10^{-3} \lesssim Z/Z_{\odot} \lesssim 10^{-2}$ at densities above a few times the cosmic mean (e.g., Tytler et al. 1995; Cowie et al. 1995; Songaila & Cowie 1996; Rauch, Haehnelt, & Steinmetz 1997; Davé et al. 1998). Since stars are thought to form in appreciable quantities only inside much denser mass condensations, the observed enrichment indicates that galaxies, which form from the IGM, also feed back some of their nucleosynthetic products in a process which is currently poorly understood but which is likely to be a crucial ingredient of galaxy formation and evolution.

Because galaxies form in relatively high-density regions, metals in low-density regions must have traveled a significant distance. This puts strong constraints on the intergalactic (IG) enrichment mechanism, therefore determining the IG metallicity at the lowest possible densities is crucial for understanding the feedback of metals from galaxies to the IGM (see, e.g., Aguirre et al. 2001; Madau, Ferrara & Rees 2001).

Previous studies, performed primarily with the Keck HIRES instrument, have used measured metal line column densities to show that, at $z \approx 3$, most absorbers with $\log N(\text{HI}) > 14.5$ (corresponding to gas overdensities $\delta \equiv \rho/\langle\rho\rangle \gtrsim 5 - 10$ [Schaye 2001]) have associated carbon lines (e.g., Tytler et al. 1995; Cowie et al. 1995;

Songaila & Cowie 1996; Ellison et al. 2000). These studies have not, however, made clear how this metallicity changes with spatial location, redshift, or gas density. Studies employing line-fitting could in principle treat the first two issues. But pushing to lower gas densities where individual metal lines are undetectable requires a statistical analysis; at high redshift this is also required for metals absorption falling blue-wards of Ly α , where the metals lines are difficult to disentangle from H I absorption.

Ellison et al. (1999, 2000; see also Cowie & Songaila 1998) have compared two ways of doing this: first by stacking the spectra of the metal-line regions corresponding to a set of low column density Ly α lines, or second by comparing the Ly α optical depth in each pixel with the optical depth in the pixel at the corresponding metal-line wavelength. The latter “pixel optical depth” (POD) method, which was devised and first used by Cowie & Songaila (1998), has several advantages: it is fast, it is objective, it preserves more of the spectrum’s information, it can be applied to heavily contaminated regions, and it appears to be more sensitive to metals in low-density gas, even in uncontaminated regions. Its shortcoming, however, has been that it is not immediately clear how to interpret the results of the POD method, and it is unclear how to convert the set of PODs into a metallicity Z at a given overdensity δ , especially when contamination is important, as for O VI (see Schaye et al. 2000a).

The purpose of the present study is to present several important improvements to and extensions of the POD

technique, to provide a complete and useful explanation of the method, and to test it using realistic spectra generated from hydrodynamic cosmological simulations. The method as described here will be applied to a sample of observed QSO spectra in a future paper. The present paper should also serve as a useful reference for prospective users of the POD technique. The testing we perform allows us to estimate the accuracy with which H I and metal line PODs can be recovered (and to refine the method for doing so), and to draw the connection between the optical depths and $Z(\delta)$ for the gas. By comparing recovered quantities directly to the true (simulated) ones, we demonstrate that the POD method does work, and that we can interpret directly the meaning of features in the POD statistic.

Section 2 contains the basics of the method, pointing forward to figures in the main text, for illustration. This section is meant for readers not interested in all the details, or as a general overview for readers unfamiliar with pixel statistics. The full details of the method, and of the tests we performed, can be found in the following sections. In § 3 we describe the simulations used in this study and how we generate spectra from them. In § 4 we give a careful account of the recovery of metal and H I PODs from QSO spectra, testing the individual steps by comparing recovered and “true” optical depths; this section can be used as a reference for the POD method of spectrum analysis, and is summarized in the Appendix. Section 5 discusses and tests the interpretation of the recovered PODs: Sections 5.1 and 5.2 relate the H I and metal PODs to the density of the absorbing gas, and § 5.3 shows the relation between metal PODs and the assumed gas metallicity, given various levels of noise and other uncertainties. In § 6 we formulate and test a procedure whereby $Z(\delta)$ can be recovered directly and perform simple tests of this procedure. Finally, we discuss our results and conclude in § 7.

2. OVERVIEW OF THE METHOD

The aim of the method is to *statistically* obtain the physical properties of the gas that produces the absorption in a given redshift range. The first step is to infer, in the presence of noise, contamination, saturation, etc., for each spectrum pixel the best possible estimate of the optical depth $\tau_{\text{Ly}\alpha}$ due to Ly α absorption by gas at some redshift, as well as the optical depths τ_Z for various metal transitions in gas at that same redshift. The second step converts the inferred optical depths to physical gas densities, using the tight relation that exists between them. This yields density ratios of H I to various metal species such as C IV and O VI. Ultimately, however, we aim to measure the metallicity as a function of overdensity. So thirdly, we use ionization corrections (as determined by the photoionization package CLOUDY), for gas at given density and temperature illuminated by a chosen ionizing background.

Simulated spectra. We use simulated spectra generated from hydrodynamical simulations to test and illustrate the method. We patch together the physical state of the gas along many uncorrelated sight-lines through the simulation box, in order to obtain one long sight-line of redshift extent $z \sim 1.5 - z_{\text{qso}}$, where z_{qso} is the assumed emission redshift of the quasar. (We illustrate the method for $z_{\text{qso}} = 2.5$ and 3.5). Metals are distributed by hand, for example by assuming a uniform metallicity of 1% solar. We

then generate simulated spectra (using our chosen ionizing background to compute ionization balances), taking into account all hydrogen Lyman transitions and absorption by important metal transitions. The wavelength extent and signal-to-noise ratio of these simulated spectra are chosen to be similar to the very high quality echelle spectra for bright quasars, as obtained by HIRES on Keck, or UVES on the VLT. Example spectra are shown in Figures 2-3.

Recovering the optical depth. The primary issue in recovering the optical depth τ from the flux $F = \exp(-\tau)$ is that information is lost when the optical depth is either too high, too low, or contaminated by other transitions. For hydrogen, we use the higher order transitions to recover the optical depth in saturated pixels. However, these higher order pixels are (potentially) contaminated by other hydrogen transitions from lower redshifts. (Note that our simulated spectra have a realistic level of this type of contamination, because they are generated from realistically long sight-lines through simulations that reproduce the observed evolution of the Ly α forest.) For hydrogen, we therefore consider only those pixels of the Lyman series which are neither too black, nor too close to the continuum. The optical depth of that redshift pixel is then the minimum optical depth of all the transitions that qualify, thereby minimizing contamination both by Lyman series lines from lower redshift, by from other transitions. Figure 1 shows how well the recovered optical depth matches the true one.

For metal transitions occurring in the Ly α forest, correcting for contamination is of course crucial. For O VI and N V, we use the Ly α optical depth determined earlier to correct for contamination by higher-order H I lines. We further reduce contamination by using the minimum optical depth for each of the components of the doublet. For C IV and Si IV, it is possible – and very important – to correct for self-contamination (i.e., where the second component of the doublet happens to fall on top of the first component of another system), and we find that an iterative correction works well (see Figure 5). On a pixel-by-pixel basis the recovery is good but imperfect, especially at low optical depth; recovered O VI and N V PODs are also systematically high, due to contamination (see Fig. 4). To obtain a statistical signal we bin the recovered metal PODs according to the corresponding hydrogen optical depth, and find the median metal POD in each bin, as illustrated, for example, in Figures 8 and 9.

These binned, recovered PODs can be further improved using the simulations. By employing simulated spectra with the same properties as the given spectrum to compute the relation between “true” and “recovered” PODs, we can “invert” the recovered PODs (which are affected by contamination, noise, etc.) to obtain an estimate of the “true” PODs in the given spectrum. This process is illustrated in Fig. 13.

From optical depth to density. In the simulations (and presumably in reality), there is a tight relation between optical depth and density, both for hydrogen (see figure 6) and for metals. These relations allow us to invert the optical depths and obtain the underlying (redshift space) densities.

Ionization corrections. To convert absorption densities to physical densities, we require ionization corrections, which depend on the shape and amplitude of the ionizing

background, as well as on the density and temperature. Fortunately, the latter two quantities are related in the simulations, and our simulations produce a temperature-density relation that is consistent with the relation measured by Schaye et al. (2000b) from the widths of Ly α lines as a function of their column density. Therefore, assuming an ionizing background (normalized to match the mean observed absorption by the IGM), we can finally deduce true physical densities of various atomic species, obtaining for example the oxygen abundance as a function of the hydrogen (over) density.

By applying this method to simulated spectra, we can estimate the importance of various physical effects and modeling uncertainties. For example, we investigate the effects of uncertainties in the temperature-density and density-column density relations, continuum fitting errors, partial wavelength coverage and noise. We demonstrate that despite these uncertainties, the algorithm is very powerful. In Figs. 13 and 14 we further show that we can accurately recover the metallicity of gas down to (at least) the cosmic mean gas density, given an accurate estimate of the ionizing background.

We conclude that relative to other techniques of analyzing absorption spectra, there are several advantages to the POD method. First, because it is not based on line fitting, the analysis is extremely fast, objective, and its implementation is straightforward. Second, it is accurate and robust because it uses the information of all transitions for each redshift pixel. Third, absorption can be detected *statistically*, enabling us to probe lower optical depths, which is crucial for studying low levels of metal contamination. We now proceed to describe and test the various steps in more detail.

3. GENERATION OF SPECTRA FROM SIMULATIONS

To test the optical depth technique we require realistic absorption spectra with wavelength range, resolution, pixel size, and noise properties similar to the observed spectra. Besides absorption by Ly α and the metal transitions of interest, the spectra must contain absorption from contaminants such as higher-order Lyman lines and additional metal lines. Before describing the procedure used to produce such spectra from a cosmological simulation, we will briefly summarize the properties of the simulation itself.

In this study we employ a hydrodynamical simulation of the currently popular flat, scale invariant, vacuum energy dominated cold dark matter model. The simulation was performed with a modified version of HYDRA (Couchman, Thomas, & Pearce 1995) and uses smooth particle hydrodynamics (SPH). The evolution of a periodic, cubic region of the universe of comoving size $12 h^{-1}$ Mpc was followed to redshift $z = 1.5$. The model has a total matter density $\Omega_m = 0.3$, vacuum energy density $\Omega_\Lambda = 0.7$, baryon density $\Omega_b h^2 = 0.019$, Hubble constant $H_0 = 65 \text{ km s}^{-1} \text{ Mpc}^{-1}$, and the amplitude of the initial power spectrum is normalized to $\sigma_8 = 0.9$. The simulation uses 256^3 gas particles and 256^3 cold dark matter particles, yielding particle masses of $2.0 \times 10^6 M_\odot$ and $1.1 \times 10^7 M_\odot$ respectively. This mass resolution has been demonstrated to be sufficient to resolve the Ly α forest spectra (Theuns et al. 1998; Bryan et al. 1999; Schaye et al. 2000b). Gas particles are converted to collisionless star particles if they

satisfy the following three conditions: (1) the density exceeds 80 times the mean baryon density; (2) the density ρ/m_H exceeds 10^{-2} cm^{-3} ; (3) the temperature is less than $2 \times 10^4 \text{ K}$. Feedback from star formation is not included. The IGM is assumed to be of primordial composition with a helium abundance of 0.24 by mass (metals are added only during the generation of spectra from the completed simulation and do therefore not contribute to the cooling of the gas). The gas is photoionized and photoheated by a model of the UV-background, designed to match the evolution of the mean Ly α absorption and the temperature-density relation measured by Schaye et al. (2000b).

The final spectra have characteristics typical of spectra taken with HIRES/KECK or UVES/VLT. The spectra span a wavelength range 3000-7500 Å and include absorption by gas from redshift $z = 1.5$ to the redshift of the QSO (z_{qso}), which is set to either 2.5 or 3.5. Absorption from Ly1 (Ly α , $\lambda 1216$) to Ly31, C III ($\lambda 977$), C IV ($\lambda \lambda 1548, 1551$), N V ($\lambda \lambda 1239, 1243$), O VI ($\lambda \lambda 1032, 1038$), Si III ($\lambda 1207$), Si IV ($\lambda 1394, 1403$), Fe II ($\lambda 1145, 1608, 1063, 1097, 1261, 1122, 1082, 1143, 1125$) is included. These transitions account for nearly all absorption by $z = 1.5$ -3.5 absorbers in the 3000-7500 Å window. Other commonly observed absorption lines, mainly from neutral and singly ionized species, occur in gas of densities higher than the maximum gas density in the simulation. However, with the exception of damped Ly α absorption, the observed spectral filling factor of this gas is small enough that the effect of these absorbers is negligible for our purposes. The simulated spectra include absorption from absorbers with $z > 1.5$ only. However, contamination by absorbers with redshift $z < 1.5$ is minimal because nearly all commonly observed absorption lines have rest wavelengths in the far UV.

At many hundreds of snapshot times, the position, density, temperature and velocity of those gas particles that affect the physical state of the gas along 6 randomly chosen sight-lines through the simulation box (i.e., those particles whose SPH smoothing kernel intersects the sight-line) are saved. The time between outputs is similar to the time it takes light to cross the simulation box. A long, continuous sight-line spanning $z = 1.5$ to z_{qso} is created by connecting short sight-lines, choosing at random from those sight-lines with redshifts close to the desired redshift. Before connecting a short sight-line it is cycled periodically so that the point at which the inferred Ly α transmission is maximum is at the ends. Since the simulation box is sufficiently large for each short sight-line to have a maximum in the Ly α transmission close to 1 (i.e., no absorption), there are generally no strong discontinuities in the long sight line. After a short sight-line has been inserted in the continuous sight-line, the gas density along the sight-line is scaled to account for the Hubble expansion during the time it takes light to cross the simulation box (this scaling is not very important because the simulation box is small). Correlations in physical quantities on scales greater than the box size are of course not modeled correctly. However, for the purpose of studying metal absorption all that matters is that the contamination by absorbers at various redshifts is modeled realistically.

The ionization balance of each gas particle is computed using the publicly available photoionization package

CLOUDY¹ (version 94; see Ferland 2000 for details), assuming the gas to be optically thin. The gas is illuminated by the redshift-dependent model of the UV/X-ray background of Haardt & Madau (1996), updated in Haardt & Madau (2001)², which includes contributions from QSOs and galaxies. The amplitude of the background radiation is scaled so that the mean Ly α absorption matches the measurements of Schaye et al. (2000b)³. The UV/X-ray background used to compute the spectra is different from the model of the background radiation that was used in the hydrodynamical simulation. The exact UV/X-ray background used in the simulation is, however, unimportant as long as the resulting thermal evolution of the IGM roughly matches the observations, which is indeed the case. The gas fraction in each ionization state (e.g., C IV/C) depends on the density, temperature, and redshift.

For each short sight-line the absorption spectra of the various transitions, i.e., the optical depths as a function of redshift, $\tau_i(z)$, are computed using the formalism described in Theuns et al. (1998). For each transition i with rest wavelength λ_i , the spectrum $\tau_i(z)$ is then added to the final, continuous spectrum $\tau(\lambda)$ using $\lambda = \lambda_i(1+z)$. The final, continuous spectrum $\tau(\lambda)$ is converted into a normalized, flux spectrum using $F = \exp(-\tau)$. It is then processed in three steps to give it characteristics similar to observed spectra taken with HIRES/KECK and UVES/VLT. First, it is convolved with a Gaussian with FWHM of 6.6 km s⁻¹ to mimic instrumental broadening. Second, it is resampled onto 0.04 Å pixels. Third, noise is added. For simplicity we have assumed the noise to be Gaussian and to consist of two components, one with flux-independent rms amplitude $(1/3)(S/N)^{-1}$ and one with amplitude $(2/3)F(\lambda)(S/N)^{-1}$, where S/N is the signal-to-noise ratio in the continuum. For most tests we quote results with both $S/N = 25$ and $S/N = 100$. Of course, when comparing with real data one should impose noise that is statistically equivalent, both in its dependence on wavelength and flux, to the noise in the observations.

To facilitate a physical interpretation of the results presented in this work, we have also computed the gas density along the continuous sight-line. Because of redshift space distortions, multiple gas elements can contribute to the optical depth of a given pixel. We therefore follow Schaye et al. (1999) and use optical depth weighted physical quantities. The density of a pixel in velocity space is defined as the sum, weighted by the contribution to its optical depth, of the density of all the gas elements that contribute to the absorption in that pixel by a given transition. Note that because different elements have different ionization corrections, the density weighted by, say, the C IV optical depth will generally differ somewhat from the density weighted by the H I optical depth, even if the metallicity is uniform. This is not an artifact of the density definition; there is no reason why the C IV and H I absorption at a given redshift should arise in exactly the same gas.

4. THE OPTICAL DEPTH TECHNIQUE

¹<http://www.pa.uky.edu/~gary/cloudy/>

²The data and a description of the input parameters can be found at <http://pitto.mib.infn.it/~haardt/refmodel.html>

³Note that the standard practice of rescaling the spectrum (i.e., multiplying the optical depth by a fixed factor) instead of the amplitude of the background radiation, could lead to large errors if absorption by metals is included.

We now describe the POD analysis method we have tested using the simulated spectra generated as described in § 3; real spectra can be analyzed in the same manner after continuum fitting and rescaling. The basic technique was pioneered by Cowie & Songaila (1998; see also Songaila 1998) and improved by Ellison et al. (2000) and Schaye et al. (2000a). In the POD method, the metal-line optical depth in each pixel is compared to the optical depth in the pixel corresponding to H I absorption by gas at the same redshift. The array of pixel pairs is then binned in H I POD, and the median metal POD in each bin computed. For a uniform density ratio of the metal ion to H I, and with perfect POD recovery, the resulting relation would be linear. In general, the detection of the metal species will manifest as a correlation between metal POD and H I PODs, and the change in the slope of this correlation indicates changes in the ratio of densities (resulting either from changes in metallicity or ionization balance with density). The utility of the POD technique relies upon an understanding of how a given physical situation maps into the recovered POD relation. Here we review the details of the method, and while doing so, compare ‘recovered’ (after noise, blending, etc.) quantities to ‘true’ (i.e., simulated) quantities where possible. We give a concise summary of our recommended implementation of the method in the Appendix.

Given a QSO redshift z_{qso} , we identify the redshift $z_{\beta} \equiv (1+z_{\text{qso}})(\lambda_{\text{Ly}\beta}/\lambda_{\text{Ly}\alpha}) - 1$ such that absorption by gas in the redshift interval $[z_{\beta}, z_{\text{qso}}]$ is uncontaminated by Ly β absorption. We will analyze pixels in the redshift range $[z_{\text{min}}, z_{\text{max}}]$ with $z_{\beta} \leq z_{\text{min}} < z_{\text{max}} \leq z_{\text{qso}}$. For a transition with rest wavelength λ_i this corresponds to a wavelength range $\lambda_i(1+z_{\text{min}}) \leq \lambda \leq \lambda_i(1+z_{\text{max}})$.

4.1. Recovery of Ly α optical depths

We derive the Ly α (1216 Å) optical depth in each pixel from the flux $F(\lambda)$ using $\tau_{\text{Ly}\alpha}(\lambda) \equiv -\ln(F)$; pixels with $\tau_{\text{Ly}\alpha} < 0$ are discarded. Pixels are considered ‘saturated’ if $F(\lambda) \leq N_{\sigma}\sigma_{\lambda}$, where σ_{λ} is the rms noise amplitude at the pixel and N_{σ} is a parameter that we vary in our tests. For saturated pixels we can recover a good estimate of the true Ly α optical depth using up to N_{ho} higher-order Lyman lines. We define $\tau_{\text{Ly}\alpha}^{\text{rec}} \equiv \min\{\tau_{\text{Ly}n}f_{\text{Ly}\alpha}\lambda_{\text{Ly}\alpha}/f_{\text{Ly}n}\lambda_{\text{Ly}n}\}$, where $f_{\text{Ly}n}$ is the oscillator strength of the n th order Lyman line and $\lambda_{\text{Ly}n}$ is its rest wavelength (Ly1= Ly α , Ly2= Ly β , etc.). We use all lines with $1 \leq n \leq N_{\text{ho}}$ that lie in the wavelength coverage of the spectrum and for which $N_{\sigma}\sigma_n \leq F(\lambda_{\text{Ly}n}) \leq 1 - N_{\sigma}\sigma_n$, where σ_n is the noise at $\lambda_{\text{Ly}n}$. The pixel is discarded if none of the available higher orders satisfies this criterion. Taking the minimum optical depth minimizes contamination by other lines, while the selection criterion picks out strong but unsaturated lines and minimizes the effects of noise. In particular, this criterion automatically excludes regions in which the noise is greater than $\sigma > (2N_{\sigma})^{-1}$.

The recovery of saturated Ly α optical depth is illustrated in Figure 1. For these and other tests we have

generated fiducial simulated spectra as described in § 3, with $z_{\text{qso}} = 3.5$ (top row) and $z_{\text{qso}} = 2.5$ (bottom row), wavelength coverage of 3000-7500 Å, 0.04 Å pixels and 6.6 km s⁻¹ detector resolution. A constant metallicity of $Z = 0.01 Z_{\odot}$ is assumed for the gas. Noise is added to each spectrum to give a signal-to-noise ratio S/N as described in § 3; for most tests we quote results with both $S/N = 25$ and $S/N = 100$, to bracket plausible, high quality observations.

All panels plot the recovered Ly α optical depth τ_{rec} vs. the ‘true’ (i.e. free of noise, instrumental broadening, and metal-contamination) value τ_{true} . The grey lines indicate the 25th(75th) percentiles of τ_{rec} .⁴ For the left two panels of the top and bottom rows of Fig. 1 we use $N_{\sigma} = 3$, $N_{\text{ho}} = 10$ and $S/N = 100$ or $S/N = 25$. The optical depth can be recovered quite reliably for $\tau_{\text{Ly}\alpha}$ up to several hundred; the errors are only slightly larger for $S/N = 25$ (second panel of top and bottom rows). The main error is a slight over-estimation of optical depth for saturated pixels, due to contamination (as shown in the bottom four panels, the effect is much smaller at $z = 2.5$ where the Ly α forest is less crowded). Note that for fixed spectral coverage, the number of higher-order lines available for reconstructing Ly α PODs depends strongly on redshift: for coverage from $\lambda \geq 3000$ Å, all higher order lines are available only for gas at $z > 2.29$, and only two higher-order lines are available for gas at $z \approx 2.1$. The middle row shows trials with the same parameters as the top-left panel, but with $N_{\text{ho}} = 1, 2, 4$, or 8; this illustrates both the effectiveness of the recovery and the importance of good spectral coverage of the higher-order lines.

In the third panels from the left (in the top and bottom rows) we show $N_{\sigma} = 1$ (with $N_{\text{ho}} = 10$, $S/N = 25$); lower N_{σ} gives less accurate recovery (the ‘bars’ extending to $\tau_{\text{true}} > \tau_{\text{rec}}$ are caused by noise), though less pixels are discarded as having no reliable optical depth estimate. Even for $N_{\sigma} = 3$ the number of discarded pixels is quite small (none at $z = 3.5$ and $\sim 10\%$ at $z = 2.5$), so we set $N_{\sigma} = 3$ in all subsequent trials unless otherwise noted.⁵

The rightmost panels (of the top and bottom rows) show the effects of errors in the continuum fit, estimated using the following procedure. We divide the spectrum into 90 Å bins with centers λ_k , and find for each bin the median flux \bar{f}_k . We then interpolate a spline across the \bar{f}_k , and flag all pixels that are at least $N_{\sigma}^{\text{cf}}\sigma$ below the interpolation. The medians are taken again using the unflagged pixels and the procedure is repeated until the fit converges. The fluxes and errors are then scaled by the fitted continuum. The accuracy of the fit depends upon $N_{\sigma}^{\text{cf}}\sigma$; fitting in highly-absorbed regions is more accurate with low N_{σ}^{cf} (because more low-flux pixels are rejected), whereas relatively unabsorbed regions are better fit with high N_{σ}^{cf} . We find that using $N_{\sigma}^{\text{cf}} = 1$ when analyzing C IV and using $N_{\sigma}^{\text{cf}} = 0.5$ for O VI gives an acceptable continuum fitting error in the metal line regions (and either value gives unimportant errors in the Ly α region). Comparison between the original and scaled spectra then shows that for $z_{\text{qso}} = 3.5$

the induced errors are $\sim +0.23 - +1.3\%$ in the Ly α region, $\sim +1.4\%$ in the O VI region and $\sim +0.06\%$ in the C IV region; for $z_{\text{qso}} = 2.5$ the errors are $\sim -0.4 - +0.4\%$, $\sim 0.1\%$, and $\sim -0.1\%$ respectively. As shown in the figure, this continuum error does not have any significant effect on the recovered Ly α optical depths; it will however, be more important in recovering the metal-line optical depths as discussed below.

4.2. Recovery of metal line optical depths

Having obtained for each pixel a good estimate of the Ly α optical depth (which, as shown below in § 5.1 can be converted into a density of the absorbing gas), we now turn to the metal-line optical depths for various species, which we will use to recover information about the metallicity of the absorbing gas.

For each pixel with $z_{\text{min}} \leq z \leq z_{\text{max}}$ we find the wavelength corresponding to absorption by some metal species, $\lambda = \lambda_i(1+z)$, where λ_i is the rest wavelength of the metal line transition; in this study we investigate the recovery of the species O VI, C IV, N V and Si IV, concentrating on the first two. The species we consider all appear in doublets (labeled here with subscripts ‘I’ and ‘II’), with the stronger transition (‘I’) twice as strong as the weaker (i.e., $f_{i,I}\lambda_{i,I} = 2f_{i,II}\lambda_{i,II}$ where f is the oscillator strength). We then compute a metal line optical depth associated with each pixel of $\tau_i(z) = \min(\tau_{i,I}(z), 2\tau_{i,II}(z))$, i.e., the minimum of the optical depth of the stronger and twice the optical depth of the weaker component of the doublet.⁶ Taking the minimum decreases contamination effects, which are particularly important for N V and O VI. Different from previous work, we do not discard pixels for which neither component is well-detected. Instead, we assign an optical depth $\tau_i(z) = -\ln(N_{\sigma}\sigma_{\lambda_{i,I}})$ (if the line is saturated) or $\tau_i(z) = \tau_{\text{min}} \equiv 10^{-5}$ (if the optical depth is negative). Because there is little scatter in metal POD at high Ly α POD, the former prescription causes $\tau_Z(\tau_{\text{HI}})$ to flatten smoothly to the highest detectable value. The latter prescription allows pixels with very low optical depth to correctly influence the median POD (the number of well-detected versus poorly-detected pixels contains information about the metallicity) as long as τ_{min} is smaller than the median in any bin, which holds for $\tau_{\text{min}} \lesssim 10^{-5}$.

Given $z_{\text{min}} > z_{\beta}$, the four chemical species we consider suffer very different levels of contamination from hydrogen lines. Carbon IV is contaminated only by other metals and by its own doublet, and Si IV is similarly uncontaminated through most of its available wavelength range. On the other hand, O VI is contaminated by several Lyman lines including Ly α , and the wavelength range for N V overlaps almost completely with that of Ly α (although there is a tiny segment with $\delta z \sim 0.1$ for which N V lies red-ward of the QSO’s Ly α emission line and is thus relatively uncontaminated). The importance of contamination can be seen in Figs. 2 and 3, which show, for $z_{\text{qso}} = 3.5$ and $z_{\text{qso}} = 2.5$ respectively, examples of a small spectrum segment in Ly α region (top panel) and the corresponding C IV (middle

⁴In each bin the 25th(75th) percentile represents the median of pixels that are below(above) a curve linearly interpolating the bin medians. They should not be interpreted as errors on the medians.

⁵For a realistic noise array in which noise increases in the far blue, somewhat more pixels are discarded because coverage of the higher-order lines is lost. Particularly at $z < 3$, this might call for a lower value of N_{σ} to maintain good statistics at large τ values.

⁶Self-contamination can be corrected (see below) in regions (such as C IV) where it is more important than contamination by other lines, and in this case the minimum should *not* be taken.

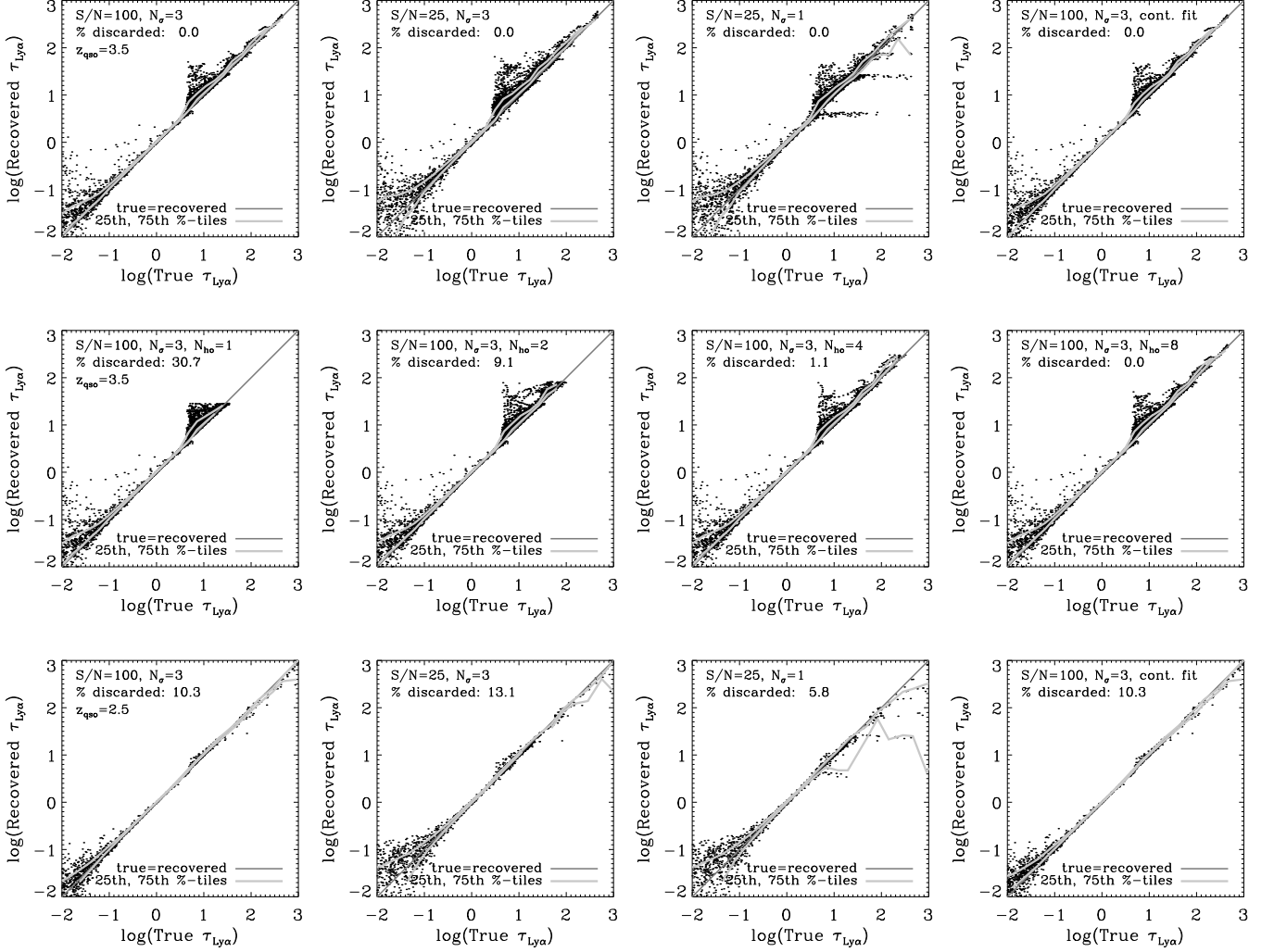


FIG. 1.— Tests of the Ly α optical depth recovery for saturated pixels, using higher-order transitions. In each panel, the ‘true’ (i.e., free of noise, contamination and instrumental broadening) optical depth τ_{true} is plotted against the optical depth τ_{rec} recovered by the analysis described in § 4.1. All of the saturated pixels and a random 10% of the rest are plotted, and the grey lines indicate 25th and 75th percentiles of recovered optical depth in each bin of true optical depth (see text). For this test we assume $z_{\text{qso}} = 3.5$ (top and middle panels) or $z_{\text{qso}} = 2.5$ (bottom panels). The left two panels of the top and bottom rows show results for 10 higher order transitions, a threshold $N_{\sigma} = 3$, and $S/N = 100$ or $S/N = 25$ in the simulated spectrum. The third panels from the left on the top and bottom rows use $N_{\sigma} = 1$. The rightmost panels on the top and bottom rows test the sensitivity to errors in the continuum (see text for details.) The middle row uses $z_{\text{qso}} = 3.5$, $N_{\sigma} = 3$, and $S/N = 100$, but its four panels show $N_{\text{ho}} = 1, 2, 4, \text{ or } 8$. We use a uniform metallicity $Z = 0.01 Z_{\odot}$, 0.04 \AA pixels, 6.6 km s^{-1} detector resolution, and a spectrum extending from $3000\text{-}7500 \text{ \AA}$, and show pixels redward of Ly β absorption.

panel) and O VI regions (bottom panel). All three panels are plotted both with and without contamination by Lyman series and metal lines.

A significant fraction of the contamination in the OVI region is due to higher-order Lyman transitions, and this contamination can be partially removed using the (accurate) estimate of the Ly α optical depth that has been computed *using* those higher-order lines as described in § 4.1. To do this, for each pixel with wavelength λ in the O VI region, we cycle through N_{corr} higher-order lines. For each line $i = 1, \dots, N_{\text{corr}}$ we check the recovered Ly α optical depth $\tau_{\text{Ly}\alpha}$ at wavelength $\lambda' = (\lambda_{\text{Ly}\alpha}/\lambda_{\text{Ly}i})\lambda$, and subtract the optical depth $\tau_{\text{Ly}\alpha}(\lambda') (f_{\text{Ly}i}\lambda_{\text{Ly}i}/f_{\text{Ly}\alpha}\lambda_{\text{Ly}\alpha})$. As can be seen in Figs. 2 and 3, this correction is quite helpful. For a given QSO redshift, the importance of this correction increases (as does H I contamination itself) with decreasing redshift of the absorbing gas, because progressively more higher-order Lyman lines contribute to the contamination.

Figure 4 shows how well the true O VI optical depths can be recovered, using a simulated spectrum. Each panel plots the median binned recovered O VI POD versus the true one (i.e. free of noise, contamination, and instrumental broadening). Top panels are for $z_{\text{qso}} = 3.5$ while bottom panels show $z_{\text{qso}} = 2.5$. The left panels show the median and 25th and 75th percentiles in recovered τ_{OVI} for our fiducial model (note that these percentiles are *not* errors in the median). There is a clear correlation between the recovered and true O VI optical depths and the recovery works particularly well at $z_{\text{qso}} = 2.5$ where there is far less contamination. We have assumed a uniform metallicity; the correlation signal would be steeper if the metallicity were to increase with density. The panels on the right show the median curves with more noise ($S/N = 25$), without correcting for contamination from higher-order Lyman lines, or with errors in the continuum fit included. Note that in both cases the continuum fitting errors work in the opposite sense from most others, *decreasing* the O VI optical depths; this effect is discussed further in § 5.3. Overall, recovery of O VI PODs is imperfect, even for fairly large τ_{OVI} , but in § 6 we shall discuss how the simulations can be used to correct for this imperfect recovery.

Self-contamination can be corrected for if it dominates other contamination, and we implement this correction for C IV. For each pixel at wavelength λ in the C IV region we check the optical depth (computed *without* taking the minimum of the doublet) at the wavelength $\lambda\lambda_{II}/\lambda_I$ where λ_I and $\lambda_{II} > \lambda_I$ are the rest wavelengths of the C IV doublet. Half this optical depth (the theoretical strength of the second doublet component) is subtracted from the initial POD estimate, and the process is iterated (and converges after about 5 iterations).

The C IV self-contamination correction works very well, but can enhance the effect of other strong contaminating lines that may be present in the C IV region of observed spectra (e.g., Mg II), by erroneously subtracting a doublet component as if they were C IV absorption. If such lines are not removed by hand, it is therefore important to remove these contaminants; this can be done automatically by discarding all pixels in the C IV region with optical

depth $\tau(\lambda)$ satisfying

$$\exp(-\tau) + 3\sigma < \exp[-2\tau(\lambda\lambda_{II}/\lambda_I) - \tau(\lambda\lambda_I/\lambda_{II})/2],$$

where σ is the r.m.s. noise of the pixels at λ , $\lambda\lambda_I/\lambda_{II}$, and $\lambda\lambda_{II}/\lambda_I$. Such pixels have too much absorption to be the sum of any doublet (with a primary component of twice the strength at $\lambda\lambda_I/\lambda_{II}$ and a primary component (with a doublet of half the strength at $\lambda\lambda_{II}/\lambda_I$), and are very likely contaminated. The self-contamination correction should then be done. We have tested this procedure by setting the flux $F = 0$ in a random fraction f of the pixels in the C IV region. For $f = 0$ the contaminant removal does not change the recovered τ_{CIV} , and with both contaminating lines and self-contamination removed as described, the recovery is not significantly affected for $f \lesssim 0.2$ (if *no* contaminant removal is done, but the minimum of the doublet components is taken, then the recovery is still only significantly affected for $f \gtrsim 0.1$) This robustness of median statistics is, of course, one of the advantages of the median POD method.

Figure 5 shows tests of the CIV recovery. As shown in the left panel, the recovery is nearly perfect down to $\tau_{\text{CIV}} \sim 10^{-3}$ at both redshifts. In the right panel, the dotted and dot-dashed curves show how the recovery becomes slightly less accurate with $S/N = 25$ or with a continuum fitting error included. Here, continuum fitting errors arise more due to noise than to significant absorption and do *not* tend to systematically reduce optical depth⁷; instead they act as an additional source of random error that reduces the accuracy of the τ_{CIV} recovery. The dashed line shows the curve without the self-contamination correction (but with the minimum of the doublet components taken); this shows that for $z_{\text{qso}} = 3.5$ and our assumed metallicity, self-contamination is the limiting factor in the C IV POD recovery if not corrected for (as was the case in previous studies).

5. TESTING AND INTERPRETING THE POD METHOD

The previous section described the recovery of metal and Ly α PODs from a simulated (or observed) spectrum, and tested the accuracy of this recovery process. In this section we use our simulations to draw connections between the recovered PODs and physical quantities such as gas density and metallicity.

5.1. Interpreting H I PODs

Previous studies – both numerical (e.g., Zhang et al. 1998, Davé et al. 1999; Croft et al. 1997,1998) and analytical (Schaye 2001) – have shown that there is a fairly tight relation between the column density or optical depth of Ly α absorption, and the density of the gas responsible for the absorption. Figure 6 confirms that a tight relation between optical depth and gas density holds on a pixel-by-pixel basis. All panels plot the median Ly α optical depth weighted overdensity versus the recovered $\tau_{\text{Ly}\alpha}$ for $z_{\text{qso}} = 3.5$ (top panels) and $z_{\text{qso}} = 2.5$ (bottom panels), using $N_{\text{ho}} = 10$ and $N_{\sigma} = 3$. The left panels show the median overdensity (dark lines) and the 25th and 75th percentiles (light lines) for $S/N = 100$. The relation is very close to a power-law, except at very low optical depth, $\tau_{\text{Ly}\alpha} \lesssim 10^{-2}$, where it flattens off. Least absolute deviation fits (dashed

⁷This is only true if N_{σ}^{cf} is carefully chosen; otherwise the continuum fitting can systematically increase or decrease the optical depth in a relatively empty region.

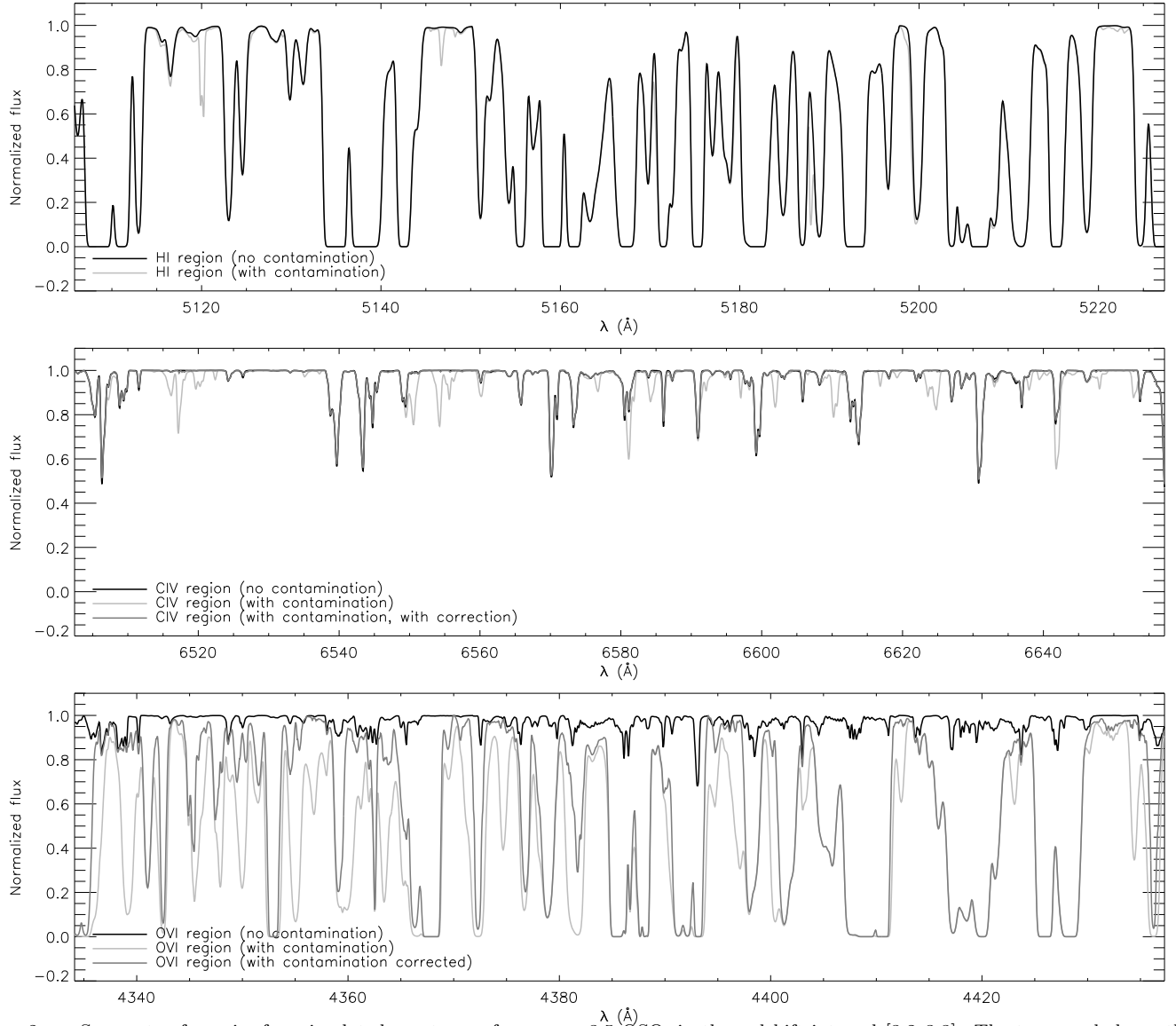


FIG. 2.— Segments of a noise-free simulated spectrum of a $z_{\text{qso}} = 3.5$ QSO, in the redshift interval $[3.2, 3.3]$. The top panel shows the Ly α region with metal contamination included (light line) and not included (dark line). The middle panel shows the corresponding region for C IV. The black line includes only the stronger doublet component, and is not contaminated by other metals (the black line is nearly invisible because the dark grey line falls almost exactly on top of it). The light line includes both doublet components and contamination (by silicon). The dark grey line shows the (contaminated) spectrum corrected for C IV *self*-contamination (see text). The lower panel's dark line is the O VI region, with all contaminants turned off. The light line shows the spectrum with H I and other metal absorption included, and the darker line shows the spectrum after removal (see text) of the higher-order Lyman lines. A uniform metallicity of $Z = 0.01 Z_{\odot}$ was used for all panels.

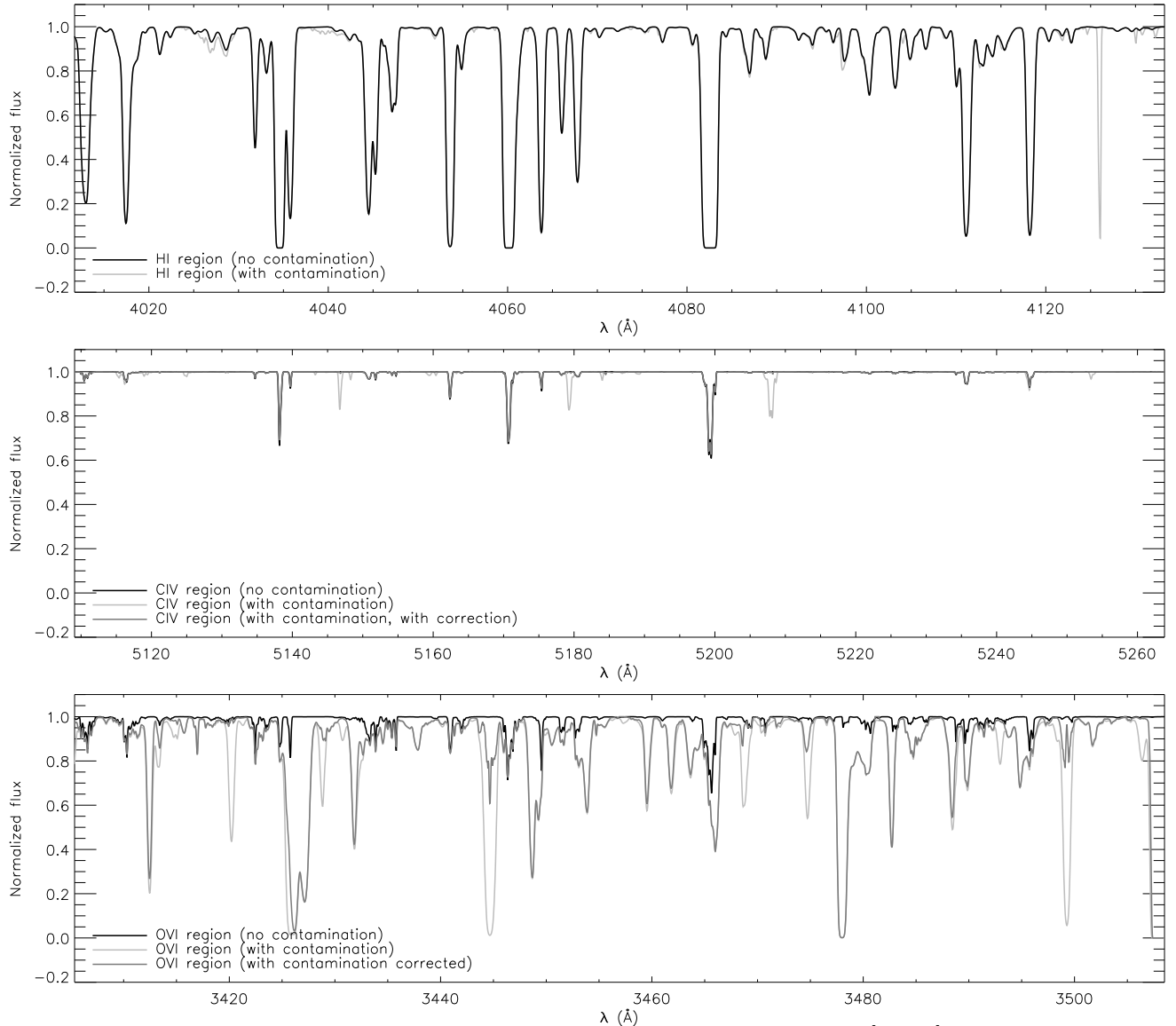


FIG. 3.— Segments of a noise-free simulated spectrum of a $z_{\text{qso}} = 2.5$ QSO, in the redshift interval $[2.3, 2.4]$ in $\text{Ly}\alpha$. Plotted lines are as in Fig. 2.

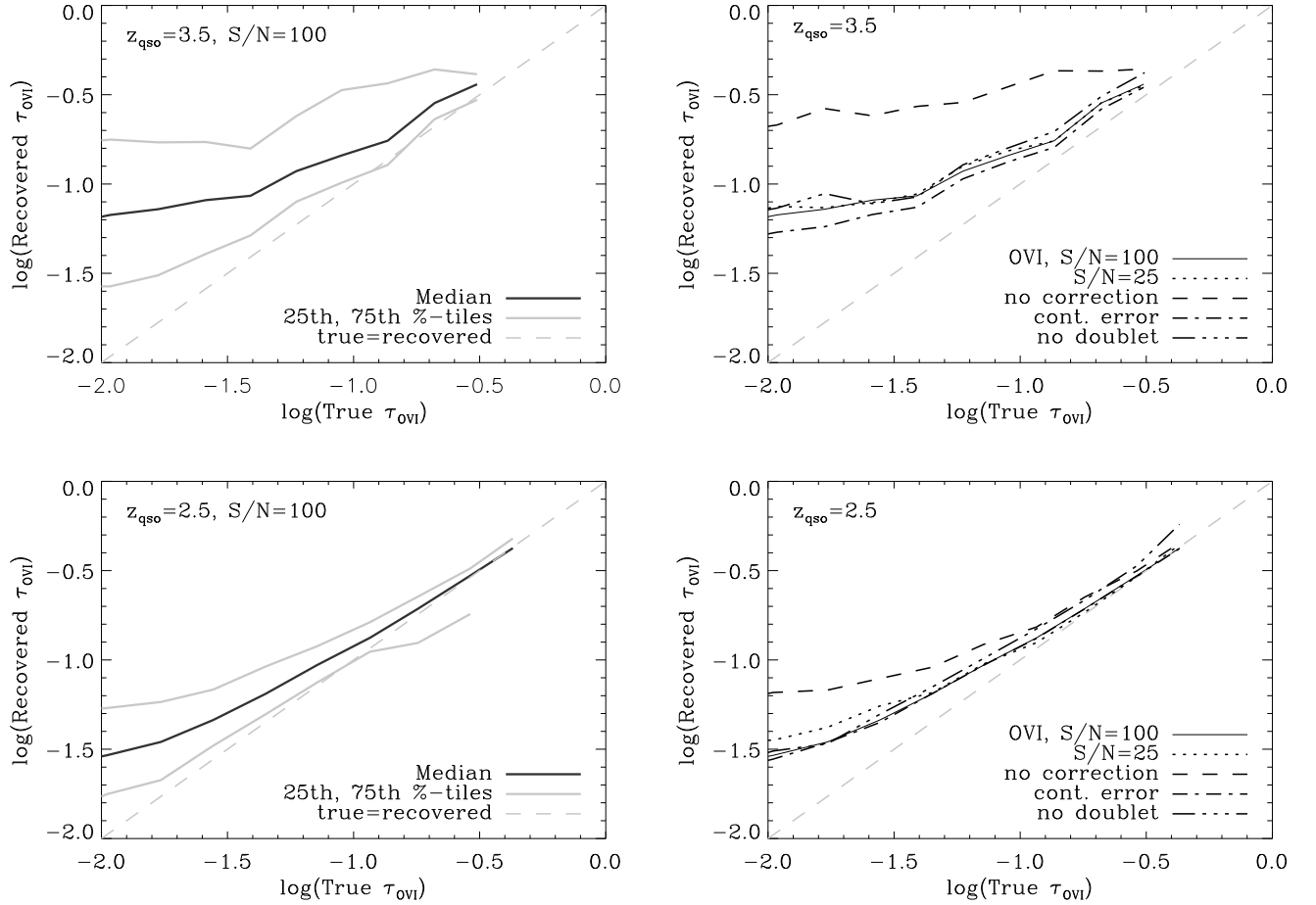


FIG. 4.— Tests of the recovery of the ‘true’ OVI pixel optical depth from the simulated spectra. The left panels show the median, 25th and 75th percentiles in recovered optical depth, versus the noise-free, perfect resolution and uncontaminated optical depth. The top panels assume $z_{\text{qso}} = 3.5$ and $[z_{\text{min}}, z_{\text{max}}] = [3.1, 3.5]$; the bottom assume $z_{\text{qso}} = 2.5$ and $[z_{\text{min}}, z_{\text{max}}] = [2.1, 2.5]$. The left panels use $S/N = 100$. The right panels (plotting only the medians) show three variations: $S/N = 25$ (dotted lines), without removal (see text) of higher-order Lyman lines from the OVI region (dashed lines), and with continuum fitting errors included (dot-dashed lines). All panels use $N_{\sigma} = 3$ and a uniform metallicity of 1% solar.

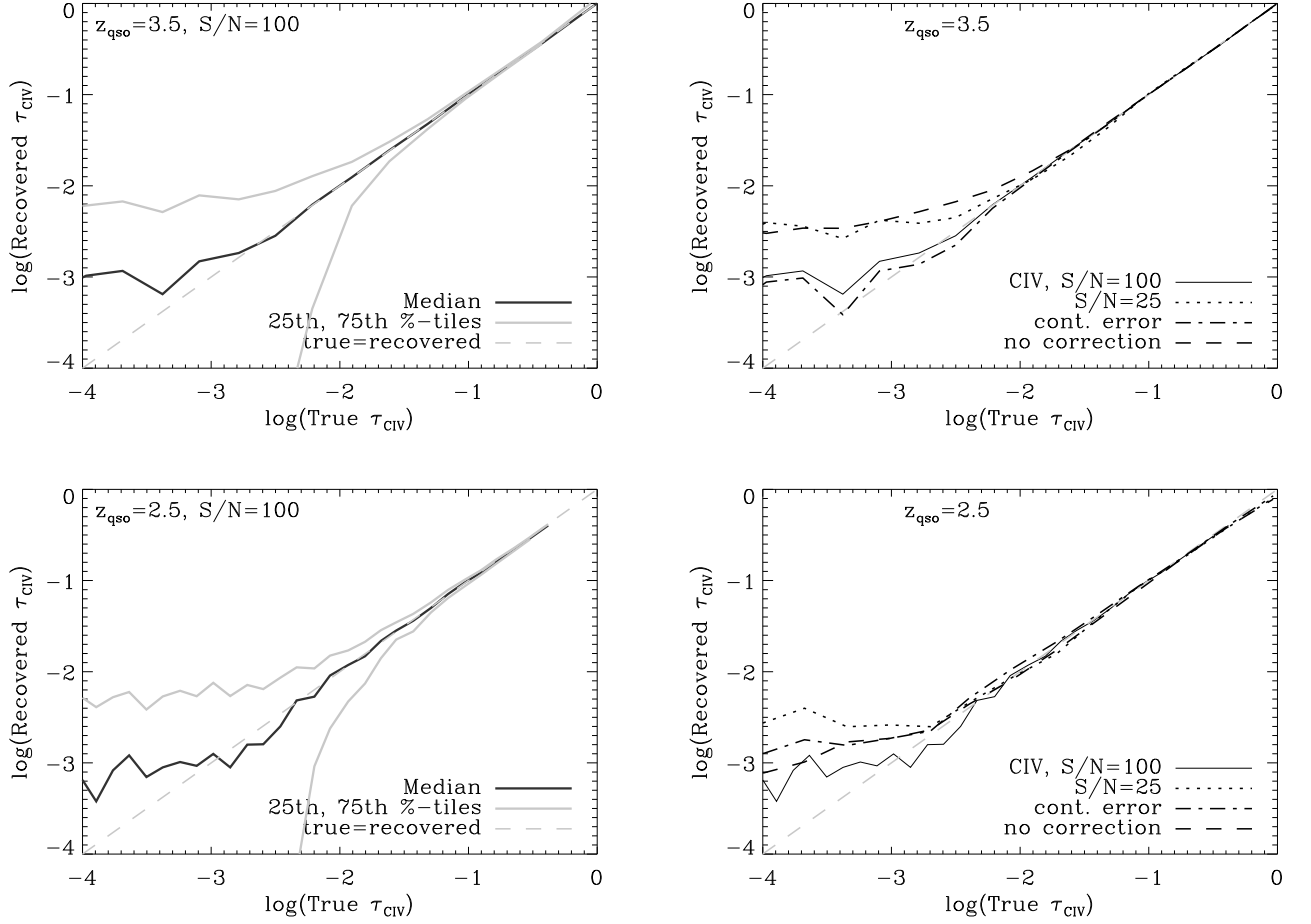


FIG. 5.— As in previous figure, but for CIV. Here, the top panels assume $z_{\text{qso}} = 3.5$ and $[z_{\text{min}}, z_{\text{max}}] = [2.8, 3.5]$; the bottom panels assume $z_{\text{qso}} = 2.5$ and $[z_{\text{min}}, z_{\text{max}}] = [1.95, 2.5]$. The three variations shown are: $S/N = 25$ (dotted lines), with continuum fitting errors included (dot-dashed lines), and without correction for self-contamination (but with the doublet minimum taken) (dashed lines).

lines) yield power-law indices of 0.60 ($z = 3.5$) and 0.68 ($z = 2.5$). Neglecting redshift space distortions, theory predicts a power-law relation of $\tau_{\text{Ly}\alpha} \propto \delta^{2.76-0.76\gamma}$, where the gas temperature obeys $T = T_0 \delta^{\gamma-1}$ (Hui & Gnedin 1997) with $1 \lesssim \gamma \lesssim 1.6$. This predicts then $\delta \propto \tau_{\text{Ly}\alpha}^\alpha$ with $0.5 \lesssim \alpha \lesssim 0.65$, in agreement with our results. The existence and tightness of this relation shows that for reasonable observational errors the density of absorbing gas can be recovered to within $\sim \pm 50\%$ about half of the time for *each* pixel, and very reliably on a statistical basis. This will allow us to readily translate information gleaned using pixel optical depths into information regarding gas of specific density (though with some uncertainty coming from uncertainty regarding the ionizing background). The right panels show medians only, for $S/N = 25$ (dotted lines), with perfect detector resolution and no noise (dashed lines), and with continuum fitting errors included (dot-dashed). These curves are all quite close except for optical depths lower than the errors (mainly due to noise).

5.2. Interpreting metal PODs

Given the tight relation between POD and gas density, the ratio of metal to Ly α PODs is related to the ratio of metal ion to H I density (subject to the errors in the recovery discussed in § 4.1), which is in turn related (by an ionization correction) to the gas metallicity. One potential pitfall in this chain of inference is that both ionization effects and the difference in the thermal widths of metal and hydrogen absorption may lead to slight offsets between the Ly α and metal lines (see Ellison et al. 2000 for some discussion). It is therefore important to test whether the absorption by metals and hydrogen arises in the *same gas* on a pixel-by-pixel basis. Figure 7 tests whether the O VI and C IV absorption in a given pixel is due to gas of the same density as the gas giving rise to the Ly α absorption. The left and middle panels plot the gas overdensity weighted by the C IV and O VI optical depth respectively (denoted by δ_{OVI} and δ_{CIV}) against the Ly α -optical depth weighted density δ_{HI} for $z_{\text{qso}} = 3.5$ (top panels) and $z_{\text{qso}} = 2.5$ (bottom panels). The correlation is good but not perfect. For high δ_{HI} the metal (and in particular the O VI) optical depth weighted densities are low compared with δ_{HI} . This effect is mainly due to the greater thermal width of the hydrogen lines (tests show that the correlation becomes very tight if the detector resolution approaches the typical Ly α line width or if the metals are given atomic weight unity so that their lines are as broad as Ly α). This discrepancy will always be unimportant for low ($\log(\delta) \lesssim 0.5$) densities, but could potentially smear the $Z(\delta)$ relation for high densities. However, as we show in § 6, this does not appear to be a significant effect, at least not for the density range over which we can measure the metallicity ($\delta_Z \lesssim 10$).

If the gas temperature is close to $\sim 3 \times 10^5$ K, then collisional ionization becomes important for O VI, and O VI is therefore often regarded as a probe of hot gas. To reach such high temperatures, the gas needs to be shock-heated. At low redshift ($z \lesssim 1$), gravitational accretion shocks may well heat a significant fraction of the baryons to temperatures $T \gtrsim 10^5$ K, but the fraction of gravitationally heated gas is predicted to be much smaller at the redshifts of interest here ($z \gtrsim 2$) (e.g., Cen & Ostriker 1999). Indeed, we find that the fraction of shock-heated gas in our

simulation is small enough for collisional ionization to be negligible. However, it should be noted that our simulations contain only gravitational shocks. If shocks from galactic winds keep a significant fraction of the high- z IGM in a hot phase, then our simulations would underestimate the fraction of collisionally ionized O VI. If this were the case then the inferred median O VI optical depth would of course still be correct. However, as mentioned in § 1, the (incorrect) assumption of pure photoionization would then lead to inaccurate conclusions concerning the oxygen abundance.

5.3. Testing the method

Having shown that the recovered Ly α optical depth is related to the gas density and that the metal absorption arises in gas with roughly the same density as the gas responsible for the hydrogen absorption, we will now investigate the relation between the measured $\tau_Z^{\text{rec}}(\tau_{\text{Ly}\alpha}^{\text{rec}})$ and the metallicity as a function of the gas density. In this section we will investigate the effects of variations in the recovery procedure and the metallicity $Z(\delta)$ on the correlation between metal and Ly α optical depth. Figures 8 and 9 show the basic results of the POD method applied to simulated spectra with uniform metallicity $Z = 0.01 Z_\odot$. Figure 8 applies the method to O VI, using fiducial parameters ($N_{\text{ho}} = 10$, $N_{\text{corr}} = 4$, and $N_\sigma = 3$). The top panels use $[z_{\text{min}}, z_{\text{max}} = z_{\text{qso}}] = [3.1, 3.5]$ while the bottom panels use $[z_{\text{min}}, z_{\text{max}} = z_{\text{qso}}] = [2.1, 2.5]$. Each panel plots $\tau_{\text{OVI}}^{\text{rec}}$ vs. $\tau_{\text{Ly}\alpha}^{\text{rec}}$, binned into 20 bins of $\log(\tau_{\text{Ly}\alpha}^{\text{rec}})$ in the range $[-3, 3]$. Dark lines indicate medians in each bin, while light lines (in left panels) signify 25th and 75th percentiles. The medians and percentiles are calculated separately for each of ten independent spectra, and the average of the medians and percentiles are plotted; the error bars about the medians in the left panels represent the standard deviation of the medians about the mean median in each bin.

The correlation between $\tau_{\text{OVI}}^{\text{rec}}$ and $\tau_{\text{Ly}\alpha}^{\text{rec}}$, which is clearly evident in the $z_{\text{qso}} = 2.5$ case for $\tau_{\text{Ly}\alpha}^{\text{rec}} \gtrsim 0.03$, indicates the detection of O VI in gas of overdensity $\delta \gtrsim 0.2$ (using Fig. 6); at $z_{\text{qso}} = 3.5$ the correlation is significant at $\tau_{\text{Ly}\alpha}^{\text{rec}} \gtrsim 0.1$, or $\delta \gtrsim 0.5$. The dashed horizontal line in each panel on the left represents the median $\tau_{\text{OVI}}^{\text{rec}}$, irrespective of $\tau_{\text{Ly}\alpha}^{\text{rec}}$. If no O VI were present, all data points would (and tests show do) lie near this horizontal line. Note that unless O VI contributes only negligibly to the mean optical depth in the metal region, this line is *not* a “reference level” (or detection limit) that gives the contribution of noise and other errors in the absence of detected metal absorption; the latter would correspond to the constant $\tau_{\text{OVI}}^{\text{ref}}$ to which the curve asymptotes as $\tau_{\text{Ly}\alpha}^{\text{rec}} \rightarrow 0$. One might hope to subtract such a “reference level” (as in Cowie & Songaila 1998) to see more clearly where metals are detected, but this requires a very accurate estimate of $\tau_{\text{OVI}}^{\text{ref}}$, and will generally lead to negative optical depths and large errors at low $\tau_{\text{Ly}\alpha}$. Thus, for practical purposes we prefer *not* to subtract the reference level, and instead recover metallicity information as described below in § 6.

The right panels show the effects of different assumptions or parameters in the analysis. The dashed lines, where no correction for higher-order Lyman lines in the O VI region was performed, show that this subtraction is quite helpful, and crucial if O VI is to be detected at $z \gtrsim 3$

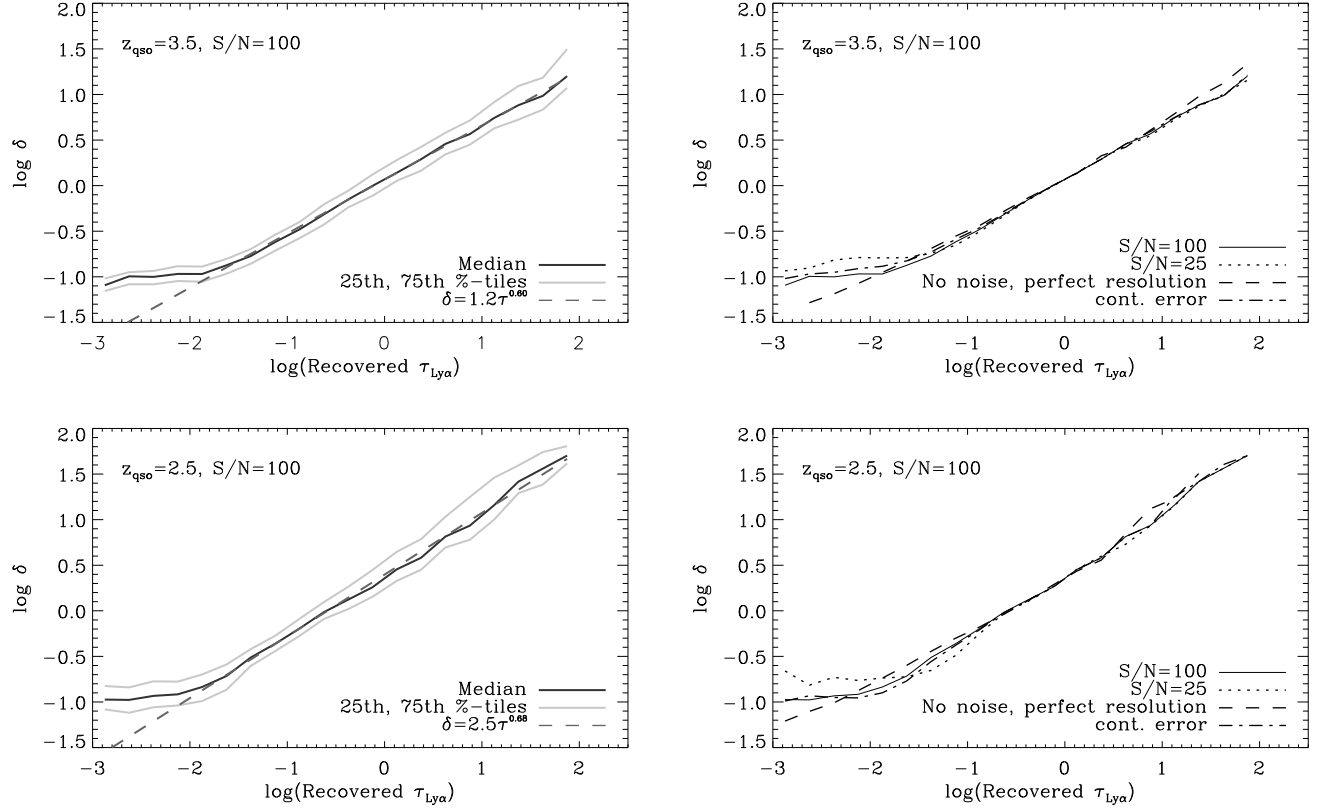


FIG. 6.— Ly α optical depth weighted overdensity of gas responsible for the absorption in each pixel, versus the recovered Ly α POD in that pixel, binned in $\tau_{\text{Ly}\alpha}^{\text{rec}}$. Left panels plot the median and 25th and 75th percentiles of gas overdensities corresponding to a given pixel optical depth; top panels show $[z_{\text{min}}, z_{\text{max}}, z_{\text{qso}}] = [2.8, 3.5, 3.5]$ while bottom panels show $[z_{\text{min}}, z_{\text{max}}, z_{\text{qso}}] = [1.95, 2.5, 2.5]$. Left panels show the fiducial $S/N = 100$ model. A least-absolute-deviation power law fit is also included and gives the relations $\delta = 1.2\tau_{\text{Ly}\alpha}^{0.60}$ ($z = 3.5$) and $\delta = 2.5\tau_{\text{Ly}\alpha}^{0.68}$ ($z = 2.5$). Right panels (showing only medians) show trials with $S/N = 25$, with continuum errors included, and with no noise and infinite detector resolution. The optical depths are recovered using up to 10 higher order lines, and $N_{\sigma} = 3$.

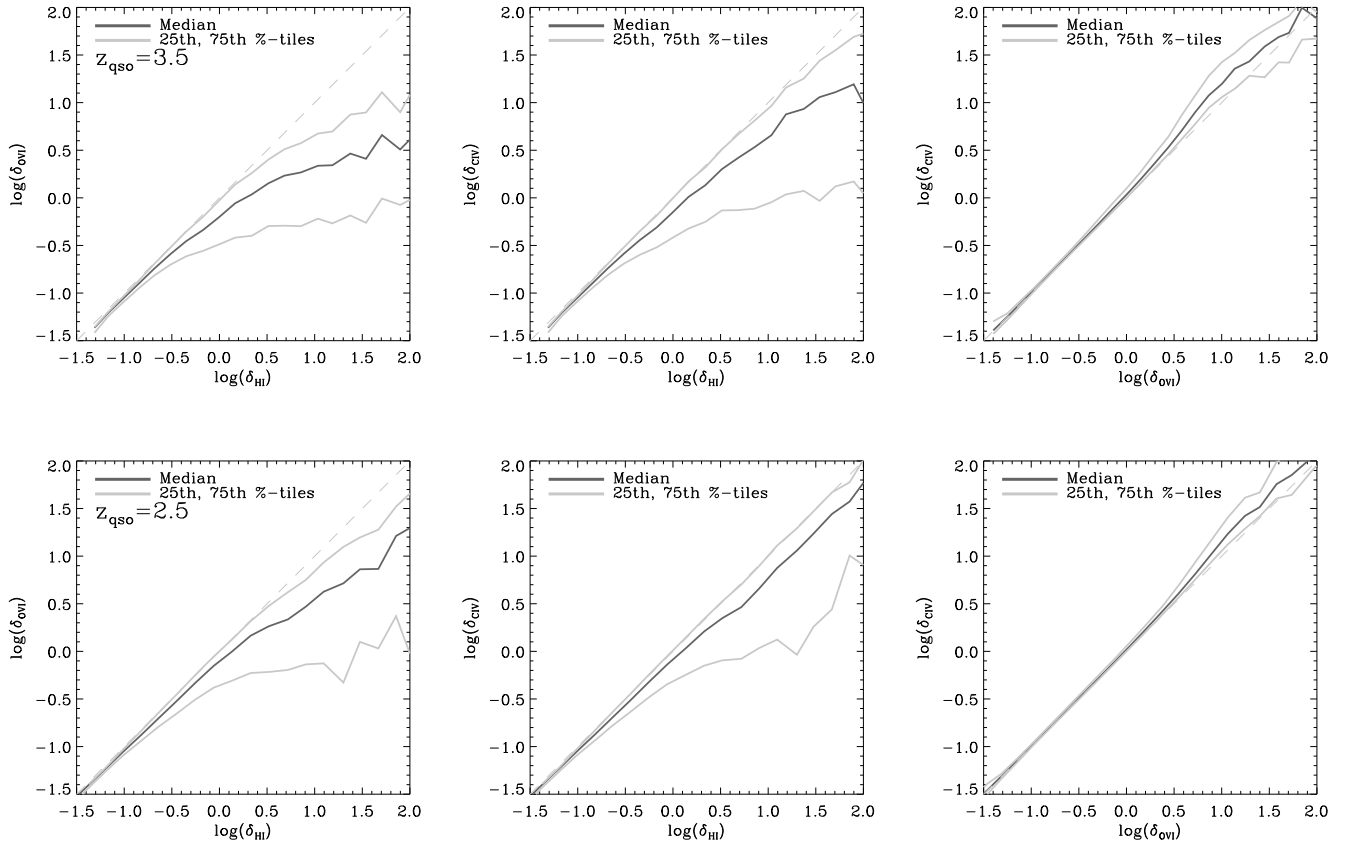


FIG. 7.— Comparison of overdensity weighted by $\tau_{\text{Ly}\alpha}$ versus that weighted by τ_{OVI} (left panels) or τ_{CIV} (middle panels), assuming $z_{\text{qso}} = 3.5$ (top panels) or $z_{\text{qso}} = 2.5$ (bottom panels). The right panels plot the two metal optical depth weighted densities against each other. Metallicity is uniform at 1% solar, and there is no noise in the spectrum.

(this correction has not been employed in previous studies). Likewise, as shown by the dot-dashed line (where the weaker doublet component is not used), taking the minimum of the doublet improves the optical depth recovery considerably. Additional noise ($S/N = 25$, dotted lines) degrades the correlation at low $\tau_{\text{Ly}\alpha}^{\text{rec}}$ for $z_{\text{qso}} = 2.5$, but has little effect for $z_{\text{qso}} = 3.5$. Probably the most dangerous effect is induced by a significant error in the continuum fit, as this *appears* to generate a false correlation by systematically decreasing O VI optical depths at small Ly α optical depths (especially for $z_{\text{qso}} = 3.5$ for which continuum fitting errors are large; see 4.1). This, however, is not as problematic as it first appears, because this effect will only slightly enhance an already-existing τ_{OVI} vs. $\tau_{\text{Ly}\alpha}$ trend; we have verified that it will not create one.

Figure 9 shows the same quantities for C IV. Again, C IV is clearly detected at very low density for $Z = 0.01 Z_{\odot}$; in this case metals are detected at $\tau_{\text{Ly}\alpha}^{\text{rec}} \gtrsim 0.06$ ($\delta \gtrsim 0.4$) for $z_{\text{qso}} = 3.5$, and at $\tau_{\text{Ly}\alpha}^{\text{rec}} \gtrsim 0.03$ ($\delta \gtrsim 0.2$) for $z_{\text{qso}} = 2.5$. Here, as in Fig. 5 above, the continuum fitting error becomes a significant random error source at very small τ_{CIV} for $z_{\text{qso}} = 2.5$, but the recovery is limited by noise for $S/N \lesssim 50$. The dashed lines show that correction for self-contamination (also not done in previous studies) is important at low optical depths.

The results of the POD analysis applied to Si IV and N V are shown in Figure 10. The left panel shows Si IV, with the usual choices of z_{qso} , and with z_{min} chosen so that only Si IV absorption redward of Ly α is used. Despite the lack of Ly α contamination, silicon is detected only at $\tau_{\text{Ly}\alpha}^{\text{rec}} \gtrsim 3$ (or $\delta \gtrsim 3$). The recovery is limited primarily by C IV contamination. Nitrogen V, shown in the right panel, can be detected well down to $\tau_{\text{Ly}\alpha}^{\text{rec}} \sim 1$ for $z_{\text{qso}} = 2.5$ but is nearly undetectable for $z_{\text{qso}} = 3.5$. The dotted line shows the analysis using $z_{\text{min}} = 2.44$ so that only the tiny region of N V absorption redward of Ly α is used. The correlation is strong, but the statistics are poor and this region is probably too close to the QSO to be of practical use. Thus, while useful information can be gleaned from the analysis of Si IV and N V PODs, they are not recoverable at as low Ly α optical depths as C IV and O VI.

The overall aim of the POD method is to recover from spectra the abundances of various metals in low-density gas. Figure 11 illustrate its effectiveness. The left panels re-plot the medians and percentiles for O VI (top) and C IV (bottom) absorption from Figs. 8 and 9 as solid lines. Dashed lines show the results for a model in which the median metallicity of the gas is still $0.01 Z_{\odot}$, but with 1 dex of scatter: the simulation is divided into cubes $0.6h^{-1}$ comoving Mpc on a side, and each is assigned a random metallicity drawn from a uniform distribution in $-3 \leq \log(Z/Z_{\odot}) \leq -1$. Compared to the uniform metallicity case, the medians are very similar (though slightly higher) and the scatter slightly larger. This indicates that the POD method can determine the overall median metallicity fairly robustly (see also Ellison et al. 2000), but cannot yield strong information about the *scatter* in the metallicity.

The right panels show trials in which the metallicity varies with gas density. Solid lines are as in the left panels, and show results for a uniform metallicity $Z = 0.01 Z_{\odot}$.

Dotted lines are trials with $Z = 0.01 Z_{\odot}$ for $\delta > 5$ and $Z = 0$ for $\delta \leq 5$. Here the τ_Z curve flattens, for both metals, at $\log(\tau_{\text{Ly}\alpha}^{\text{rec}}) \approx 0 - 0.3$ (or $\delta \approx 4 - 6$), confirming that the correlation vanishes at HI optical depths roughly corresponding to densities at which there are no metals. The difference between the solid and dotted lines at $0.2 \lesssim \log(\tau_{\text{Ly}\alpha}^{\text{rec}}) \lesssim 0.7$ does, however, indicate that the presence of metals at $\delta < 5$ affects metal PODs corresponding to HI PODs with $\log(\tau_{\text{Ly}\alpha}) > 0$. The dashed line shows a trial with $Z = 0.001 Z_{\odot}$. For carbon the curve is quite similar to that for $Z = 0.01 Z_{\odot}$, scaled down by ~ 1 dex; for O VI the signal is quite washed out even for larger $\tau_{\text{Ly}\alpha}$. Finally, the dot-dashed line is for metallicity $Z = 0.001\delta Z_{\odot}$. For C IV this curve roughly matches the $Z = 0.01 Z_{\odot}$ curve at $\log(\tau_{\text{Ly}\alpha}) \approx 0.8$ ($\delta \approx 13$), and matches the $Z = 0.001 Z_{\odot}$ curve for $\log(\tau_{\text{Ly}\alpha}) \sim -1$ ($\delta \sim 1$), as one would hope (though in the latter case the values are determined by the noise). The trend of increasing metallicity with gas density is apparent in the steep slope of the dot-dashed line in the C IV plot, but the difference in slope between this model and the constant 1% metallicity model with a cutoff is not very apparent for O VI.

The results of this section show that the interpretation of the median pixel optical depth is reasonably straightforward *as long as* noise and other systematic errors are small (as for C IV) but becomes somewhat more ambiguous when contamination or self-contamination are important (as for O VI). In the next section we describe how simulated spectra, which map “true” to “recovered” optical depths, can be used to directly invert the pixel optical depths into C IV/H I and O VI/H I ratios as a function of gas density.

6. RECOVERING $Z(\delta)$

In the preceding sections, we described, tested, and improved the basic POD recovery method that has been used previously in analyses of absorption spectra. Despite our improvements, these recovered PODs are still somewhat affected by contamination, noise, etc. With our simulated spectra it is, however, possible to extend the basic method by using the relation – derived from the simulations – between true and recovered PODs, to recover a good estimate of the true metal PODs from observations. Furthermore, if we use the simulations to determine the relations between density and Ly α optical depth, and between density and temperature, and if we assume a fixed ionizing background radiation, then we can correct for the ionization of both the metal and hydrogen and convert the ratio $\tau_Z/\tau_{\text{Ly}\alpha}(\tau_{\text{Ly}\alpha})$ into a metallicity as a function of density. In this section we describe and test this procedure.

6.1. Correcting the optical depth using simulations

Figures 4 and 5 show examples of recovered vs. true pixel optical depths in O VI and C IV, for particular sets of parameters describing the simulated spectrum, and for a metallicity $Z(\delta, z) = \text{const} = 0.01 Z_{\odot}$ of the gas as a function of overdensity and redshift. Given the relation $\tau_Z^{\text{rec}}(\tau_Z^{\text{true}})$ for a spectrum simulated to have the same properties as an observed spectrum, the binned recovered metal PODs (such as those shown in figs. 8-11) can be “inverted” to yield “true” PODs, significantly removing the

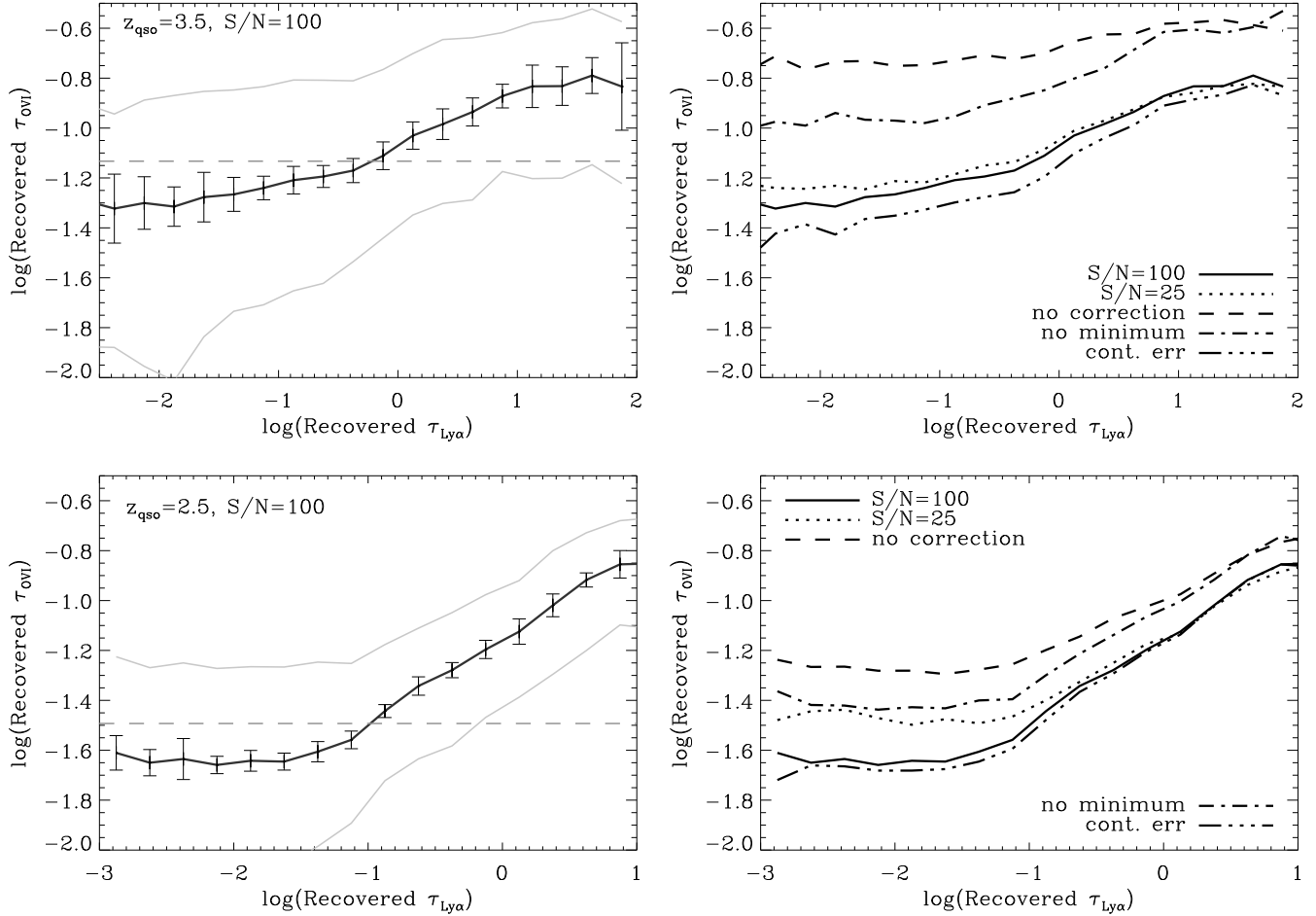


FIG. 8.— Recovered OVI optical depth vs. recovered Ly α optical depth for $z_{\text{qso}} = 3.5$ (top panels) and $z_{\text{qso}} = 2.5$ (bottom panels). Left panels assume a uniform metallicity $Z = 0.01 Z_{\odot}$, $z_{\text{min}} = 3.1$, $z_{\text{max}} = z_{\text{qso}}$, $N_{\sigma} = 3$, and $S/N = 100$. The median and 25th and 75th percentiles are averaged over ten independent spectra, and the error bars represent the standard deviations of the medians about the mean median. The horizontal dashed lines indicate the median τ_{OVI} , irrespective of $\tau_{\text{Ly}\alpha}$. Right panels show mean medians for the fiducial model (solid lines) and various other models: with $S/N = 25$ (dotted lines), without correction for higher-order Lyman lines (dashed lines), without taking the minimum of the doublet, (dot-dashed line), or with continuum fitting error included (triple-dot-dashed lines).

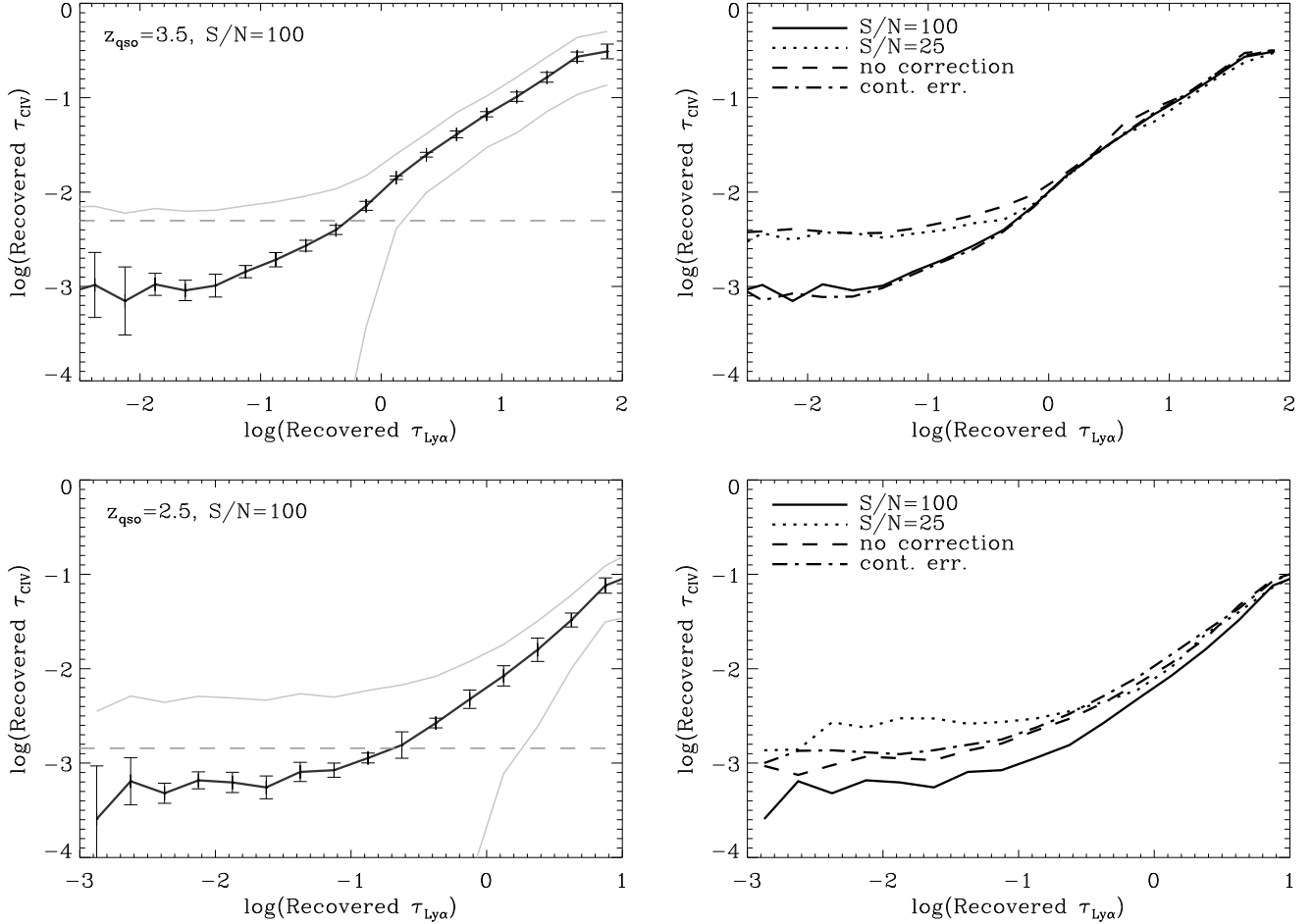


FIG. 9.— Recovered CIV optical depth vs. recovered Ly α optical depth for $z_{\text{qso}} = 3.5$ (top panels) and $z_{\text{qso}} = 2.5$ (bottom panels). Left panels assume uniform metallicity $Z = 0.01 Z_{\odot}$, $z_{\text{min}} = 3.1$, $z_{\text{max}} = z_{\text{qso}}$, $N_{\sigma} = 3$, and $S/N = 100$. The median and 25th and 75th percentiles are averaged over ten independent spectra, and the error bars represent the standard deviations of the medians about the mean median. The horizontal dashed lines indicate the median τ_{CIV} , irrespective of $\tau_{\text{Ly}\alpha}$. Right panels show mean medians for the fiducial model (solid lines) and various other models: with $S/N = 25$ (dotted lines), without self-contamination correction (dashed lines), or with continuum fitting errors included (dot-dashed lines).

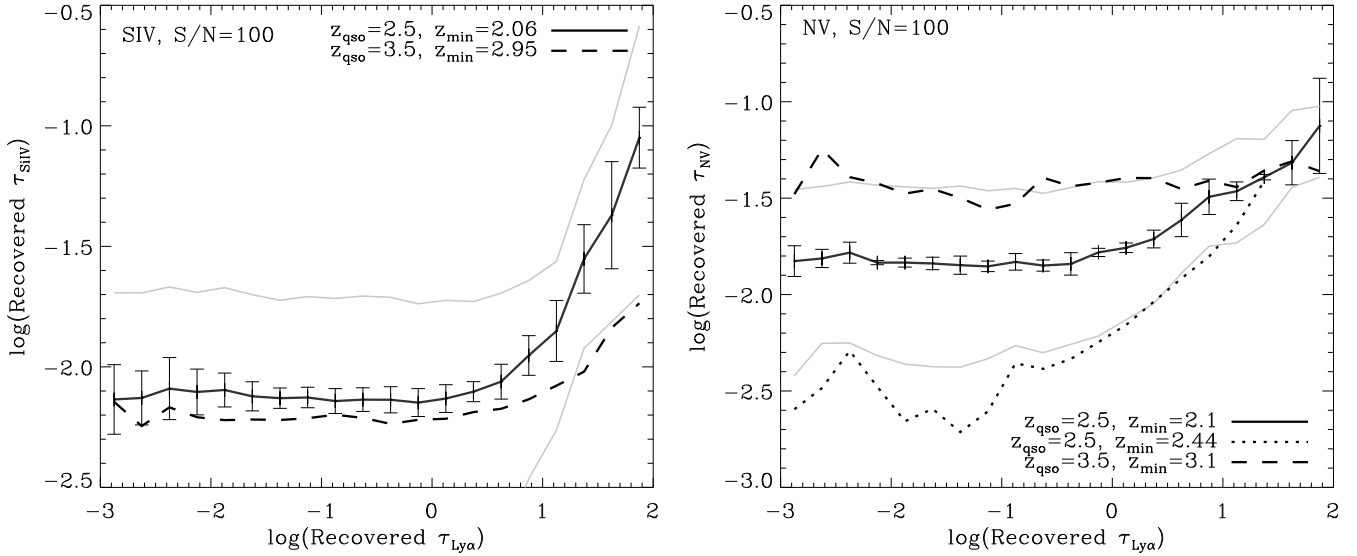


FIG. 10.— Recovered SiIV (left panel) or NV (right panel) optical depth vs. recovered Ly α optical depth. The metallicity is uniform at $0.01Z_{\odot}$. Solid lines show results for $z_{\text{qso}} = 2.5$, with $z_{\text{min}} = 2.06$ (SiIV) or $z_{\text{min}} = 2.1$ (NV), while dashed lines show results for $z_{\text{qso}} = 3.5$, with $z_{\text{min}} = 2.95$ (SiIV) or $z_{\text{min}} = 3.1$ (NV). The dotted line in the NV (right) panel uses $z_{\text{qso}} = 2.5$, $z_{\text{min}} = 2.44$, which includes only NV pixels redward of Ly α . For all curves $z_{\text{max}} = z_{\text{qso}}$.

effects of noise, thermal broadening, contamination by H I, and continuum fitting errors. The remaining effects of self-contamination and contamination by other metal lines, if important, can also be corrected for *provided* the metallicity used in the simulated spectra (which are in turn used to perform the inversion) is similar to the metallicity in the observations.

Figure 12 exhibits tests of the importance of metal line contamination for the recovery of true optical depths for O VI (left panels) and C IV (right panels), for $z_{\text{qso}} = 3.5$ (top panels) and $z_{\text{qso}} = 2.5$ (bottom panels). Curves of $\tau_Z^{\text{rec}}(\tau_Z^{\text{true}})$ are plotted for several different choices of $Z(\delta)$. With the exception of O VI at $z = 2.5$, the curves are virtually identical in their overlap region, indicating that the deviation from perfect recovery is dominated by factors other than metal line contamination (O VI at $z = 2.5$ has a significant level of self-contamination; recall that self-contamination was removed for C IV). If the curves are independent of metallicity within the range of τ_Z^{rec} recovered from the analyzed spectrum, the inversion can be done in one step; if the assumed metallicity affects the $\tau_Z^{\text{rec}}(\tau_Z^{\text{true}})$ obtained, the inversion can still be done using an iterative approach, as discussed below.

The basic inversion procedure is demonstrated in Fig. 13, which illustrates the process applied to C IV in a $z_{\text{qso}} = 2.5$ spectrum with fiducial parameters. Given $\tau_{Z,k}^{\text{rec}}(\tau_{\text{Ly}\alpha,k}^{\text{rec}})$ in bins k (panel 1) and the monotonic (hence invertible) curve $\tau_Z^{\text{rec}}(\tau_Z^{\text{true}})$ fit through the binned pixels (panel 2), we are able to compute $\tau_{Z,k}^{\text{inv}}(\tau_{\text{Ly}\alpha,k}^{\text{rec}}) \equiv \tau_Z^{\text{true}}[\tau_{Z,k}^{\text{rec}}(\tau_{\text{Ly}\alpha,k}^{\text{rec}})]$ (hereafter we drop the index k of the bin). The $\tau_Z^{\text{rec}}(\tau_Z^{\text{true}})$ relation, which we compute by averaging over 10 spectra, is indeed monotonic but increasingly flat at low τ_Z^{true} . We therefore determine a value $\tau_{Z,\text{min}}^{\text{rec}}$ (and $\tau_{Z,\text{min}}^{\text{true}}$) (shown in light, dotted lines in panels 2 and

3) below which the curve is effectively flat, and determine an “error” σ_{min} on this value by computing the standard deviation of the median optical depth across the ten realizations for all of the pixels with $\tau_Z^{\text{true}} < \tau_{Z,\text{min}}^{\text{true}}$. The curve also varies from one realization of the spectrum to the next; these variations are quantified in each bin by the standard deviation of the 10 averaged realizations, and two more monotonic functions $\tau_Z^{\text{rec},\pm}(\tau_Z^{\text{true}})$ can be constructed using the $\pm 1\sigma$ values. The median, $\pm 1\sigma$, and $\pm 2\sigma$ values of τ_Z^{rec} are then inverted into τ_Z^{inv} : the median values are inverted using the mean $\tau_Z^{\text{rec}}(\tau_Z^{\text{true}})$, while the -1σ and -2σ values are inverted using the $\tau_Z^{\text{rec},+}(\tau_Z^{\text{true}})$ curve and the $+1\sigma$ and $+2\sigma$ values are inverted using the $\tau_Z^{\text{rec},-}(\tau_Z^{\text{true}})$ curve. As for the “flat” part of the recovered spectrum, we set $\tau_Z^{\text{inv}} = 0$ when $\tau_Z^{\text{rec}} < \tau_{Z,\text{min}}^{\text{rec}}$, and set the $\pm 1\sigma$ and $\pm 2\sigma$ values to zero when they fail to exceed $\tau_{Z,\text{min}}^{\text{rec}} \mp \sigma_{\text{min}}$. Projecting the errors this way ensures that: A) we have included a conservative estimate of the error induced by variance in the true vs. recovered POD relation from one realization of the spectrum to the next, and B) the flattening of $\tau_Z^{\text{rec}}(\tau_Z^{\text{true}})$ correctly manifests as large negative errors (effectively upper limits) in τ_Z^{inv} for low values of $\tau_{\text{Ly}\alpha}^{\text{rec}}$.

The result of this procedure is shown in panel 3. The plotted points are our best estimates of the true, uncontaminated τ_Z versus $\tau_{\text{Ly}\alpha}$. These will be reliable to the degree that errors in the recovered PODs are dominated by noise or H I contamination, which should be correctly modeled by the simulations. If the errors are dominated by continuum fitting errors, the inversion procedure should be correct for this if the same continuum fitting procedure is used (with equal effectiveness) on the simulated and real spectra. If (as for O VI at low- z) self-contamination is important, the inverted PODs will be accurate only if the

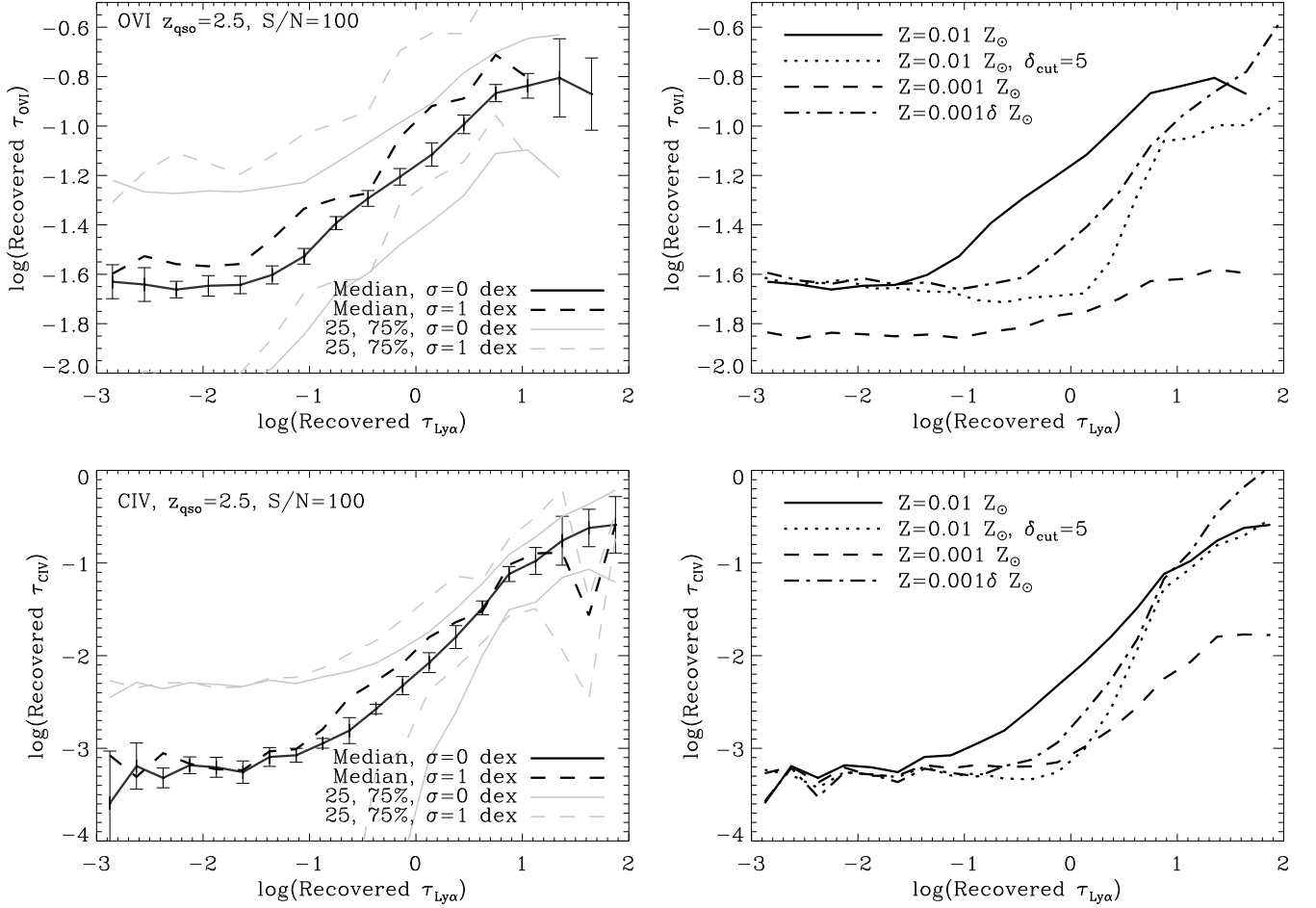


FIG. 11.— Recovered metal optical depth vs. recovered Ly α optical depth for OVI (top panels) and CIV (bottom panels) for different metallicity distributions. Left panels use a *median* metallicity $Z = 0.01 Z_{\odot}$, but one trial with a uniform metallicity (solid lines), and one in which there is a 1 dex scatter in $\log(Z)$ on ~ 1 Mpc scales (dashed lines). The right panels show trials in which the metallicity is constant at $Z = 0.01 Z_{\odot}$ (solid) or $Z = 0.001 Z_{\odot}$ (dashed), a trial in which $Z = \text{const.}$ for overdensity $\delta > \delta_{\text{cut}} = 5$ and zero otherwise (dotted), and a trial in which $Z = 0.001\delta$ (dot-dashed). All panels have $z_{\text{qso}} = 2.5, S/N = 100, N_{\sigma} = 3, N_{\text{H0}} = 10$ and $N_{\text{CORR}} = 4$.

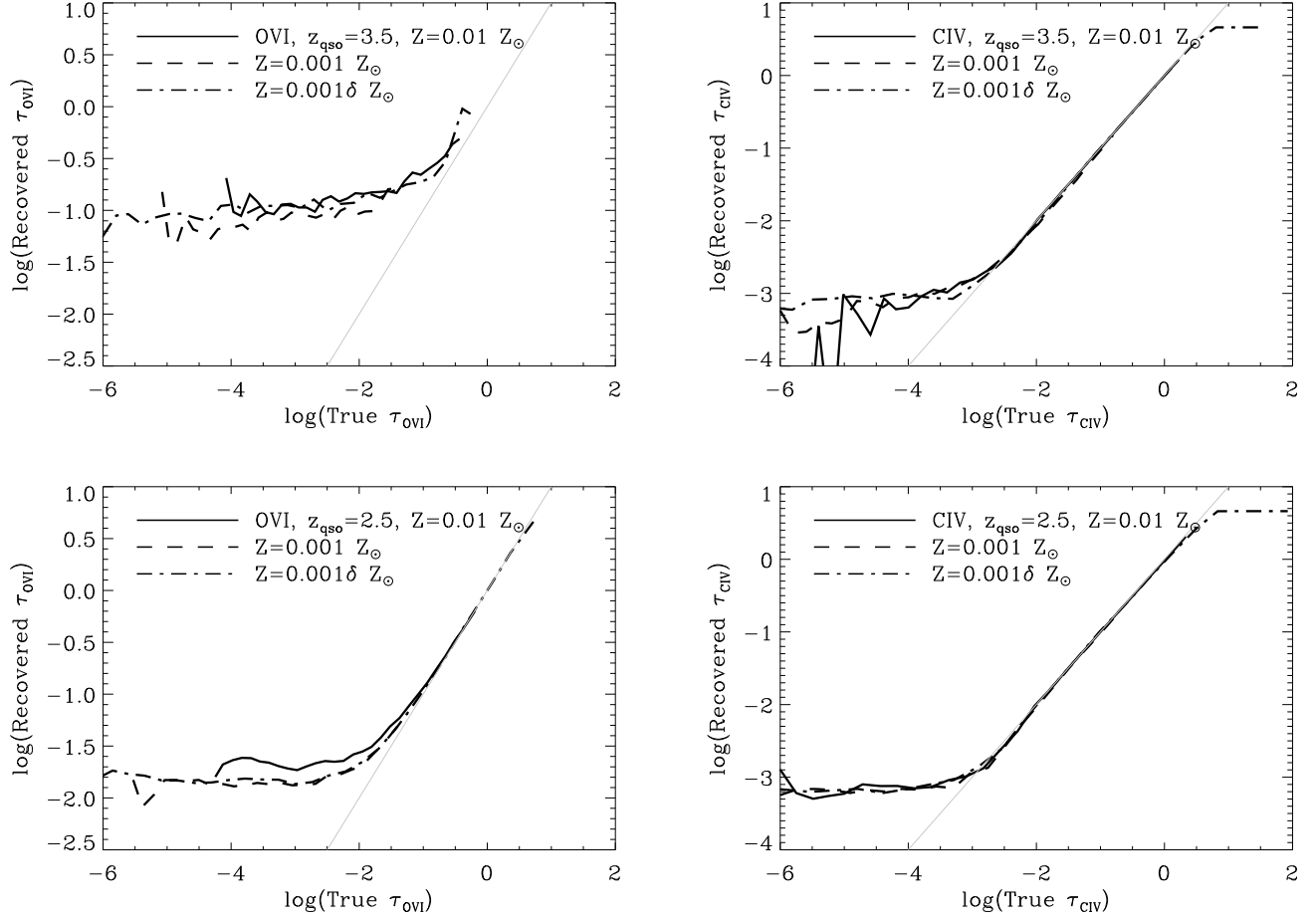


FIG. 12.— Test of the recovery of the pixel optical depth from the simulated spectra, for different metallicities. Left panels show OVI, while right panels show CIV. Top (bottom) panels have $z_{\text{qso}} = 3.5(2.5)$. Recovered vs. true POD is plotted for uniform metallicities of $10^{-3} Z_{\odot}$, $10^{-2} Z_{\odot}$, and $Z = 0.001 \delta Z_{\odot}$. The light solid line indicates perfect recovery. The flattening at high τ_{CIV} is due to saturation.

level of metal contamination in the spectra used in the inversion is similar to that in the real spectrum.

6.2. Interpreting the optical depth ratios

As mentioned in § 5, the simulations can be further used to interpret the PODs in terms of the metallicity $Z(\delta, z)$ of the absorbing gas.

First, the ratio of the metal to H I optical depth can be converted into the ratio of the metal ion to H I density, both as a function of the H I optical depth. For example, for C IV we can compute for each bin,

$$\frac{n_{CIV}}{n_{HI}} = \frac{\tau_Z^{\text{inv}}(f\lambda)_{HI}}{\tau_{Ly\alpha}^{\text{rec}}(f\lambda)_{CIV}}.$$

Second, the tight relations between gas density and Ly α optical depth, and between temperature T and density, give for each bin in Ly α optical depth, a density and temperature of the corresponding absorbing gas, denoted respectively by $\delta_{Ly\alpha}(\tau_{Ly\alpha}^{\text{rec}})$ and $T_{Ly\alpha}(\tau_{Ly\alpha}^{\text{rec}})$. These are shown (solid lines) in panels 4 and 5 for our example inversion. Given an assumed ionizing background, these can then be used to compute, for each bin, an ionization correction $n_H(n_{HI})$ to yield a physical H I density of absorbing gas for each bin. Third and similarly, the binned, *metal* optical-depth-weighted density and temperature, $\delta_Z(\tau_{Ly\alpha}^{\text{rec}})$ and $T_Z(\tau_{Ly\alpha}^{\text{rec}})$ (panels 4 and 5, dotted lines) can be used to correct for the ionization of the metal, to yield an estimate of the density n_i of the atomic species i ($i = \text{C}, \text{O}, \text{etc.}$).⁸

The ratio n_i/n_H then represents a true metallicity of species i for each bin, yielding (using $\delta_Z[\tau_Z^{\text{rec}}]$) an estimate of $Z(\delta_Z)$. The metallicities in our sample inversion are shown in panel 6, with the dark dashed line representing the true metallicity. The good agreement between the measured and true metallicities demonstrates the effectiveness of the procedure (even when the metallicity used to derive $\tau_Z^{\text{rec}}(\tau_Z^{\text{true}})$ is different from the true metallicity) when the ionizing background is taken to be the same as used in the spectrum generation.

The solid and (light) dashed lines indicate the changes in recovered metallicities induced, respectively, by an overall scaling of $\pm 50\%$ in temperature or density used in the ionization correction; these are conservative estimates of how much the temperature and density in the simulations could differ from those of the true IGM. Such variations induce only small changes in the inferred metallicity compared with the statistical errors.

More uncertain is the shape and spatial variation of the ionizing background, and the importance of collisional ionization (collisionally ionized gas would have very different ionization corrections than photoionized gas); here we have used the model of the UV-background from quasars and galaxies of Haardt and Madau (2001), and used simulations without feedback from star formation (i.e., only gravitationally induced shocks are included) so that the fraction of collisionally ionized gas is negligible for the redshifts of interest here. The effects of changes in the

assumed ionizing background radiation can be studied by varying the background used in the inversion, but we will not do this here.

After the recovery of metallicities $Z(\delta)$, the inversion can be checked or if necessary iterated, as follows. A new set of simulated spectra can be generated using the metallicity found in the inversion,⁹ and used to generate a new $\tau_Z^{\text{rec}}(\tau_Z^{\text{true}})$ (panel 2). Using this new relation the inversion can be repeated. If the results are consistent with the first iteration, then the recovery was *not* significantly affected by metal-line contamination. If the first two iterations differ, the procedure can be repeated until convergence is obtained.

After convergence, the measured metallicity $Z(\delta)$ can again be used to generate new simulated spectra. Comparison of the pixel statistics (e.g., $\tau_Z^{\text{rec}}(\tau_{Ly\alpha}^{\text{rec}})$) for these spectra and the original spectra then provides a strong consistency check on the recovered metallicity, the simulation assumptions, and the observed spectrum.

The top two panels of Fig. 14 show the results of the inversion procedure applied to C IV for $z_{\text{qso}} = 3.5$ (left panel), and for $z_{\text{qso}} = 2.5$ with a true metallicity $Z = 0.001\delta Z_{\odot}$ (right panel). The first shows that for $z_{\text{qso}} = 3.5$ the inversion is able to constrain the metallicity of even underdense gas (we find that this holds for $Z \gtrsim 0.001 Z_{\odot}$); the second demonstrates that the inversion can cleanly recover a trend in $Z(\delta)$. (Note that the $z_{\text{qso}} = 3.5$ examples use only about half of the available redshift range; it is worth noting that here – and in general – this does not significantly increase the error bars.) The bottom two panels show the inversion applied to O VI, for $z_{\text{qso}} = 2.5$ (left panel) and $z_{\text{qso}} = 3.5$ (right panel). Despite contamination by H I, O VI serves as a good tracer of metallicity for $z_{\text{qso}} = 2.5$, even in slightly underdense gas. For $z_{\text{qso}} = 3.5$ the inversion is not as accurate as for C IV, but can still yield a good constraint on the metallicity of overdense gas.

7. DISCUSSION AND CONCLUSIONS

Studies of the absorption spectra of QSOs at $2 \lesssim z \lesssim 4$ have revealed that the intergalactic medium is enriched with metals to the level of $\sim 0.1 - 1\%$ solar metallicity at overdensities $\delta \gtrsim 5$. However, a more accurate estimate of the metallicity and its spatial variation, as well as the extent to which it varies with gas density and redshift, are currently unknown. This paper is the first in a series that systematically analyzes a sample of QSO absorption spectra in an effort to glean as much information as possible about the enrichment of low-density gas at high redshift.

In the present paper, we have systematically described, tested, and discussed the “pixel optical depth” (POD) method of analyzing metal absorption in QSO spectra. This method, while still less widely used than direct line-fitting techniques, is better able to extract information from low-density regions in which individual metal lines are difficult or impossible to detect. The POD technique

⁸We find that using Ly α -weighted quantities to correct for H ionization and metal-weighted quantities to correct for metal ionization works slightly better than using either set of quantities in both corrections.

⁹In practice this may be done by performing a power-law or geometric fit to the recovered $Z(\delta)$. If self-contamination is important, the inversion is inaccurate if the metallicity assumed in performing the inversion is very different from the true metallicity. This effect appears chiefly for τ_Z below the dashed line in panel 1 (since, as mentioned in § 5.3, this line indicates the level below which the metal contributes significantly to the absorption). Thus, in the first iteration we fit $Z(\delta)$ only using points with τ_Z above this dashed line.

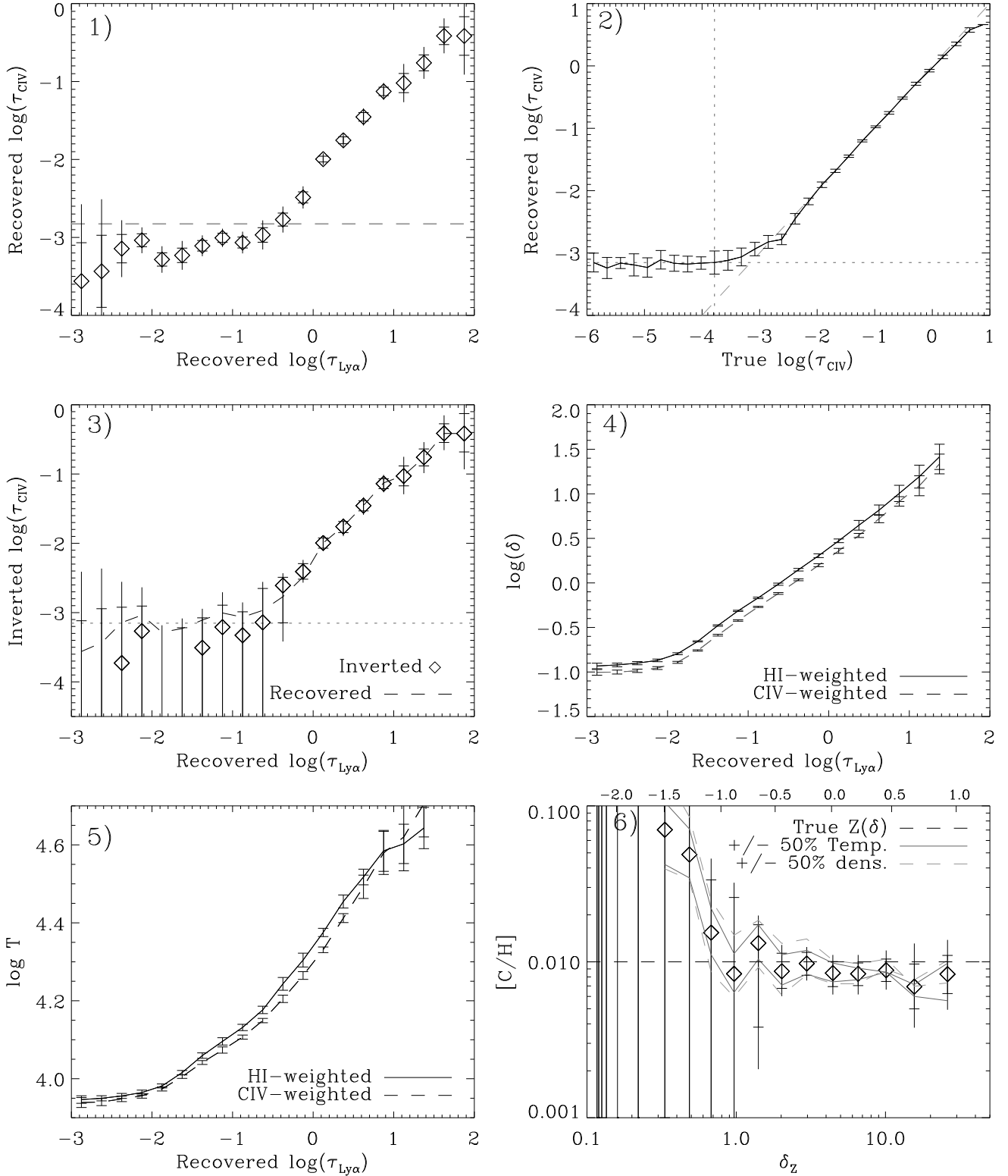


FIG. 13.— Test of the recovery of gas metallicity versus density. Here, $z_{\text{qso}} = 2.5$ and we recover carbon. The analyzed spectrum has $Z = 0.01 Z_{\odot}$, whereas the spectra used in performing the inversion use $Z = 0.001\delta Z_{\odot}$. **Panel 1:** $\tau_{\text{CIV}}^{\text{rec}}$ versus $\tau_{\text{Ly}\alpha}^{\text{rec}}$ (diamonds). 1- and 2- σ errors determined using bootstrap resampling are shown. **Panel 2:** The median binned ‘true’ vs. ‘recovered’ metal POD relation. Errors are computed by taking the standard deviations among 10 independent spectra. The horizontal (vertical) light dotted line indicates the recovered (true) τ_{CIV} value below which the relation is taken to be flat. **Panel 3:** ‘Inverted’ metal PODs using panels 1 and 2, as described in text. Dotted line is as in panel 2. The dashed line re-plots the relation of panel 1 for comparison. **Panel 4:** $\text{Ly}\alpha$ (solid line) and metal (dashed line) optical depth weighted overdensity of absorbing gas vs. recovered $\text{Ly}\alpha$ POD. Errors are computed as in panel 2. **Panel 5:** As panel 3 but for temperature. **Panel 6:** Recovered carbon abundance in solar units versus metal optical depth weighted density, given an ionization correction using density and temperature from panels 3 and 4, and the same ionizing background as was used in the generation of the spectra. The true metallicity is plotted (dashed line). Solid and light dashed lines indicate, respectively, changes induced by an overall $\pm 50\%$ scaling in temperature or density in the ionization correction.

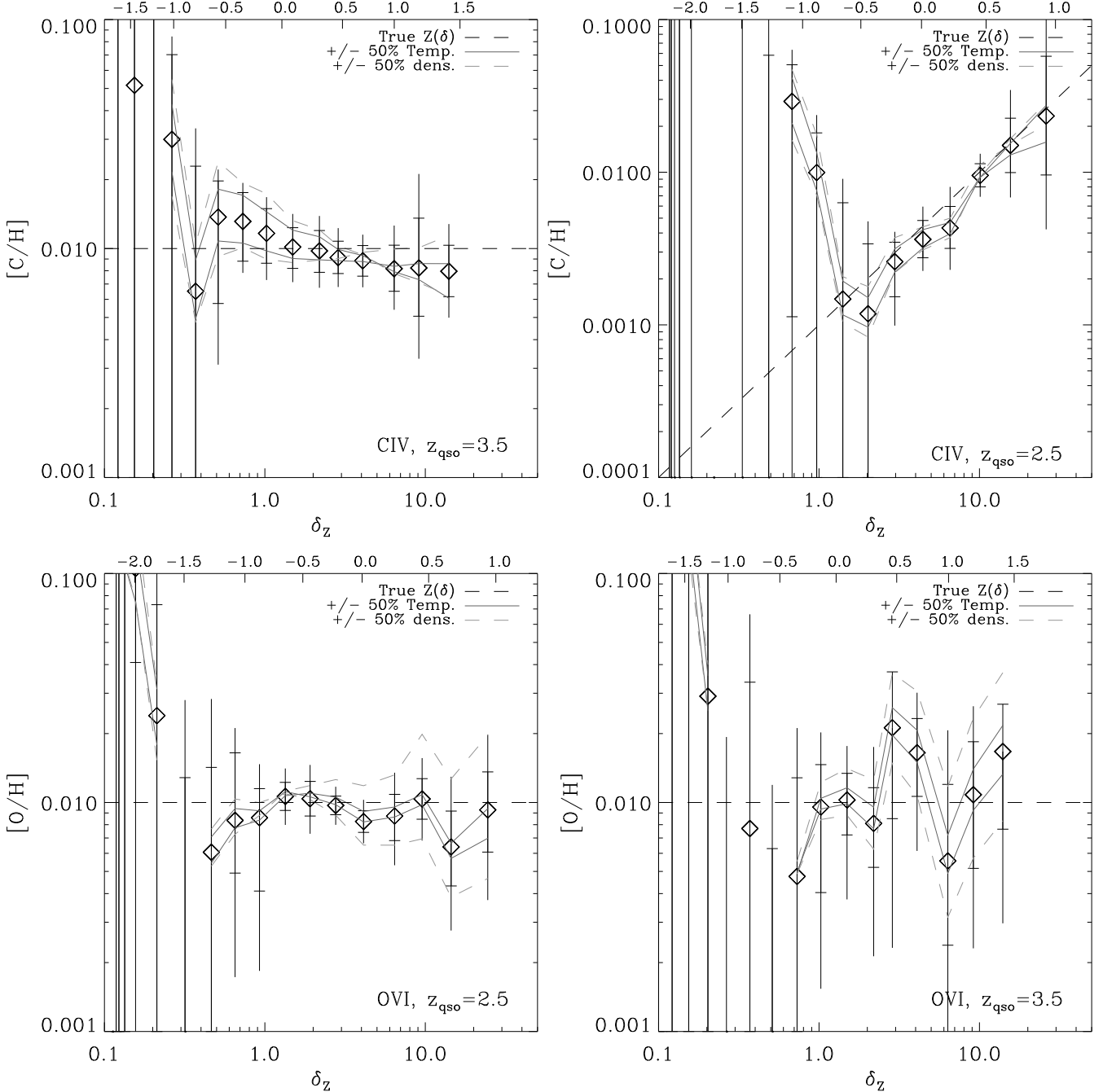


FIG. 14.— As panel 6 of the previous figure, but for different elements or metallicities. **Top left:** CIV inversion for $z_{\text{qso}} = 3.5$, with $z_{\text{min}} = 3.3$. **Top right:** CIV inversion for $z_{\text{qso}} = 2.5$, but with $Z = 0.001\delta Z_{\odot}$ in the analyzed spectrum, and $Z = 0.01 Z_{\odot}$ in the spectra used for the inversion. **Bottom left:** OVI inversion for $z_{\text{qso}} = 2.5$. **Bottom right:** OVI inversion for $z_{\text{qso}} = 3.5$, with $z_{\text{min}} = 3.3$.

was developed and previously employed in QSO absorption studies of C IV (Cowie & Songaila 1998; Ellison et al. 2000) and O VI (Schaye et al. 2000a), but has suffered from difficulties in the interpretation of the results. Here we overcome this difficulty by testing the method on spectra generated from realistic cosmological hydrodynamical simulations that are able to reproduce the observed statistics of the Ly α forest.¹⁰ This has allowed us to both assess the effectiveness of the method, and to refine and calibrate it. The major improvement to the method developed and tested here is the removal of higher-order Lyman lines from the O VI region, and the correction of self-contamination of C IV by its own doublet. These innovations significantly improve the accuracy of the O VI and the C IV recovery. In the Appendix we gave a compact but complete recipe for implementing the method.

The most general result of our tests is that the POD technique is very effective at recovering information about the metallicity of low-density gas, even where (as for O VI) the metal lines are severely contaminated. More specifically, our tests reveal the following:

1. Ly α optical depths of up to several hundred can be reliably determined using higher order Lyman lines, and these optical depths in turn give an accurate estimate of the density of gas giving rise to the absorption.
2. With high-quality spectra (signal-to-noise $\gtrsim 50$) median C IV optical depths binned in Ly α optical depth can be accurately recovered down to $\tau_{\text{CIV}} \sim 10^{-3}$ for both $z_{\text{qso}} = 3.5$ and $z_{\text{qso}} = 2.5$. Previous analyses were probably limited by self-contamination; with our correction for this effect, the recovery is limited by noise and by errors in the continuum fitting.
3. The recovery of median O VI PODs is limited primarily by contamination due to H I lines (and secondarily by continuum fitting errors). A significant fraction of this contamination can be removed, allowing a fairly accurate recovery of O VI PODs with $\tau_{\text{OVI}} \gtrsim 10^{-2}$ for $z_{\text{qso}} = 2.5$, and a useful recovery of median PODs for $z_{\text{qso}} = 3.5$.
4. The Si IV (limited primarily by C IV contamination) and N V (limited primarily by Ly α contamination) PODs can be usefully recovered for Ly α optical depths ($\tau_{\text{Ly}\alpha} \gtrsim 1$).
5. Using the POD method both C IV and O VI should be detectable in realistic spectra of $z \sim 3$ QSOs even in gas of the mean cosmic density, if the metallicity is $\sim 10^{-3} Z_{\odot}$, and at even lower density if the metallicity is higher.

6. When applied to simulated spectra with different metallicities as a function of gas density, the method is able to distinguish models in which the metallicity is constant from those in which the metallicity declines significantly with gas density. The results are *not* very sensitive to spatial variations in metallicity at a given gas density.
7. Most important for accurate recovery of metallicity information are large wavelength coverage (so that a significant number of higher order Lyman lines can be used), accurate continuum fitting, and high signal-to-noise. However very high S/N is only useful for C IV recovery; obtaining a $S/N \gg 50$ probably does not significantly improve the amount of information that can be recovered regarding O VI.
8. Due to different levels of thermal broadening in metals vs. hydrogen, the inferred density/temperature of the gas is, somewhat different when weighted by metal line optical depth than when weighted by Ly α optical depth, especially at relatively high gas densities. However, this uncertainty does not appear to significantly affect the derived metallicities.
9. Using spectra generated from cosmological simulations, the POD method may be extended, as described in § 6, to directly and accurately recover the metallicity of intergalactic gas vs. its density. The largest uncertainty in this “inversion” is the spectral shape (and possible spatial variations) of the ionizing background. For a given background, the abundances of C and O can be measured with errors of at most a factor of a few over at least an order of magnitude in density, using a single high-quality spectrum.

The POD technique, as refined and calibrated in our study should, when applied to QSO spectra of currently-available quality, yield clear information about the metallicity of even underdense gas. This information will place strong constraints on models of the enrichment of the IGM, and consequently on feedback and galaxy formation.

AA and JS are supported in part by a grant from the W.M. Keck Foundation. TT thanks PPARC for the award of an Advanced Fellowship. Research was conducted in cooperation with Silicon Graphics/Cray Research utilizing the Origin 2000 super computer at DAMTP, Cambridge.

REFERENCES

- Aguirre, A., Hernquist, L., Schaye, J., Weinberg, D. H., Katz, N., & Gardner, J. 2001, ApJ, 560, 599
- Bryan, G. L., Machacek, M., Anninos, P., & Norman, M. L. 1999, ApJ, 517, 13
- Cen, R. & Ostriker, J. P. 1999, ApJ, 514, 1
- Couchman, H. M. P., Thomas, P. A., & Pearce, F. R. 1995, ApJ, 452, 797
- Cowie, L. L. & Songaila, A. 1998, Nature, 394, 44
- Cowie, L. L., Songaila, A., Kim, T., & Hu, E. M. 1995, AJ, 109, 1522
- Croft, R. A. C., Weinberg, D. H., Katz, N., & Hernquist, L. 1998, ApJ, 495, 44
- Croft, R. A. C., Weinberg, D. H., Katz, N., & Hernquist, L. 1997, ApJ, 488, 532
- Davé, R., Hellsten, U., Hernquist, L., Katz, N., & Weinberg, D. H. 1998, ApJ, 509, 661

¹⁰It should be noted that this is *all* that is required of the simulations, i.e., the results of this paper are not dependent upon the detailed accuracy of the cosmological simulations, but only on the simulations’ proven ability to roughly match observed QSO absorption spectra.

- Davé, R., Hernquist, L., Katz, N., & Weinberg, D. 1999, *ApJ*, 511, 521
- Ellison, S. L., Lewis, G. F., Pettini, M., Chaffee, F. H., & Irwin, M. J. 1999, *ApJ*, 520, 456
- Ellison, S. L., Songaila, A., Schaye, J., & Pettini, M. 2000, *AJ*, 120, 1175
- Ferland, G. J. 2000, *Rev. Mexicana Astron. Astrofis. Ser. Conf.*, 9, 153
- Haardt, F. & Madau, P. 1996, *ApJ*, 461, 20
- Haardt, F., & Madau, P. 2001, to be published in the proceedings of XXXVI Rencontres de Moriond, astro-ph/0106018
- Hui, L. & Gnedin, N. Y. 1997, *MNRAS*, 292, 27
- Madau, P., Ferrara, A., & Rees, M. J. 2001, *ApJ*, 555, 92
- Rauch, M., Haehnelt, M. G., & Steinmetz, M. 1997, *ApJ*, 481, 601
- Schaye, J. 2001, *ApJ*, 559, 507
- Schaye, J., Theuns, T., Leonard, A., & Efstathiou, G. 1999, *MNRAS*, 310, 57
- Schaye, J., Rauch, M., Sargent, W. L. W., & Kim, T. 2000a, *ApJ*, 541, L1
- Schaye, J., Theuns, T., Rauch, M., Efstathiou, G., & Sargent, W. L. W. 2000b, *MNRAS*, 318, 817
- Songaila, A. 1998, *AJ*, 115, 2184.
- Songaila, A. & Cowie, L. L. 1996, *AJ*, 112, 335
- Theuns, T., Leonard, A., Efstathiou, G., Pearce, F. R., & Thomas, P. A. 1998, *MNRAS*, 301, 478
- Tytler, D., Fan, X.-M., Burles, S., Cottrell, L., Davis, C., Kirkman, D., & Zuo, L. 1995, *QSO Absorption Lines*, Proceedings of the ESO Workshop Held at Garching, Germany, 21 - 24 November 1994, edited by Georges Meylan. Springer-Verlag Berlin Heidelberg New York.
- Zhang, Y., Meiksin, A., Anninos, P., & Norman, M. L. 1998, *ApJ*, 495, 63.

APPENDIX

SUMMARY OF THE METHOD

The POD method as we have described and tested above can be implemented as follows, given an absorption spectrum of a QSO at redshift z_{qso} .

1. **Choose redshift range.** Determine $z_\beta \equiv (1 + z_{\text{qso}})(\lambda_{\text{Ly}\beta}/\lambda_{\text{Ly}\alpha}) - 1$, and choose a redshift range $z_\beta \leq z_{\text{min}} < z_{\text{max}} \leq z_{\text{qso}}$. For a given transition i with rest wavelength λ_i , pixels with wavelength $\lambda_i(1 + z_{\text{min}}) \leq \lambda \leq \lambda_i(1 + z_{\text{max}})$ can then be analyzed without Ly β contamination of the Ly α region.
2. **Derive Ly α PODs.** Take $\tau_{\text{Ly}\alpha}(z) \equiv -\ln(F)$ where $F(\lambda)$ is the observed normalized flux at $\lambda = \lambda_{\text{Ly}\alpha}(1 + z)$; mark as “discarded” pixels with $\tau_{\text{Ly}\alpha} < 0$.

If $F(\lambda) \leq 3\sigma_\lambda$ (where σ_λ is the normalized noise array), the pixel is saturated. For these pixels, find the minimum of the Ly α optical depth corresponding to the optical depth seen in the available higher-order lines: define

$$\tau_{\text{Ly}\alpha}^{\text{rec}} \equiv \min \{ \tau_{\text{Ly}n} g_{\text{Ly}\alpha} / g_{\text{Ly}n} \},$$

where $g_{\text{Ly}n} \equiv f_{\text{Ly}n} \lambda_{\text{Ly}n}$, $f_{\text{Ly}n}$ is the oscillator strength of the n th order Lyman line and $\lambda_{\text{Ly}n}$ is its rest wavelength. Compute this, using as many higher-order lines as fall within the spectrum’s coverage, use only pixels that are not “poorly detected”, i.e., use those for which $3\sigma_n \leq F \leq 1 - 3\sigma_n$ (where σ_n is the noise at $\lambda_{\text{Ly}n}$). If no higher-order lines are usable, mark the pixel as discarded.

3. **Derive metal PODs.** Consider the spectral region covering all multiplet components of the metal in question for redshift $z_{\text{min}} \leq z \leq z_{\text{max}}$. Then find the optical depth in all multiplet components, that is, compute $\tau_{Z,k}(z)$ by using the flux at wavelengths $\lambda_{Z,k}(1 + z)$ where $\lambda_{Z,k}$ is the rest wavelength for the k th multiplet component of the metal species (relevant lines appear in doublets with $k = 1, 2$). If the flux $F < 3\sigma_{\lambda_{Z,k}(1+z)}$, the line is effectively saturated; in that case set $\tau_Z(z) = -\ln(3\sigma_{\lambda_{Z,k}(1+z)})$.

A. Correct the metal PODs for higher-order Lyman contamination. If the metal lines lie in a region shared with higher-order Lyman lines (as is the case for O VI), subtract this contamination using an interpolation of the $\tau_{\text{Ly}\alpha}^{\text{rec}}$ values derived in step 2, as follows (otherwise skip to step C):

$$\tau_{Z,k}(z) := \tau_{Z,k}(z) - \sum_{n=2} \frac{g_{\text{Ly}n}}{g_{\text{Ly}\alpha}} \tau_{\text{Ly}\alpha}^{\text{rec}}(\lambda \lambda_{\text{Ly}\alpha} / \lambda_{\text{Ly}n}),$$

where $\lambda = \lambda_{Z,k}(1 + z)$, and the sum is over the higher-order lines with wavelength covered by the spectrum. Do this for each multiplet component k . Skip now to step C.

or B. Correct the metal PODs for contamination and self-contamination. For lines without Lyman-series contamination, and in which self-contamination is dominant (such as C IV), self-contamination may be corrected using the following procedure.

First correct for contamination by other strong lines: find all pixels with

$$\exp[-\tau_Z(\lambda)] + 3\bar{\sigma} < \exp[-(g_2/g_1)\tau(\lambda_s) - (g_1/g_2)\tau(\lambda_d)],$$

where $g_k \equiv f_{Z,k} \lambda_{Z,k}$, $\lambda = \lambda_{Z,1}(1 + z)$, $\lambda_d = \lambda_{Z,2}(1 + z)$, $\lambda_s = (\lambda_{Z,1}/\lambda_{Z,2})\lambda$, and $\bar{\sigma} = (\sigma_{\lambda_s}^2 + \sigma_{\lambda_d}^2 + \sigma_\lambda^2)^{1/2}$ is the quadrature sum of the noises at λ_s , λ_d , and λ . Since the optical depth at λ should be the sum of a primary component (with a doublet of strength g_2/g_1 at λ_d) and a doublet (with a primary component of strength g_1/g_2 at λ_s), the selected pixels are then very likely contaminated; discard them so that they are used neither in the analysis nor in the self-contamination correction.

Then, correct for self-contamination using the following algorithm:

1. Begin with the optical depths of the primary component:

$$\tau_Z^{\text{rec}}(\lambda) = \tau(\lambda), \quad \lambda \equiv \lambda_{Z,1}(1 + z).$$

2. Subtract the doublets corresponding to these optical depths:

$$\tau_Z^{\text{rec}}(\lambda) := \tau(\lambda) - (g_2/g_1)\tau_Z^{\text{rec}}(\lambda \lambda_{Z,1}/\lambda_{Z,2}).$$

(The values of τ_Z^{rec} at the specified wavelengths must be interpolated from those available; for wavelengths lying outside of the available range, take optical depths from the original full spectrum.)

3. Repeat the second step until convergence occurs (approximately four more iterations). The resulting $\tau_Z^{\text{rec}}(z)$ is well-corrected for self-contamination.

C. Take minimum of doublet If self-contamination is *not* being corrected (i.e. step B was skipped), take $\tau_Z(z) = \min\{g_k^{-1}\tau_{Z,k}(z)\}$ using only those components $k > 1$ for which $\tau_{Z,k} > 0$. As above, $g_1 = 1$, $g_k/g_1 \equiv f_{Z,k}\lambda_{Z,k}/f_{Z,1}\lambda_{Z,1}$, and $f_{Z,k}$ is the oscillator strength (for O VI, C IV, N V and Si IV, $g_1 = 1$, $g_2 = 2$). If $\tau_Z(z) < 0$, set $\tau_Z(z)$ to some fixed value (e.g., 10^{-5}) much smaller than the noise.

4. **Bin the Ly α and metal PODs.** Create bins of $-3 \lesssim \log(\tau_{\text{Ly}\alpha}^{\text{rec}}) \lesssim 2$ and compute the median $\tau_{\text{Ly}\alpha}$ and τ_i in each bin. Errors can be computed by bootstrap resampling: divide the analyzed region into 5 – 10 \AA chunks (the chunk size should be greater than the line widths), then compute a large number of realizations in which enough chunks are randomly selected (each chunk may be selected multiple times) and concatenated to form a spectrum with a number of pixels equal to the original. Bin each realization, and take as the error in each bin the standard deviation from the mean median.